Dust emission and transport associated with a Saharan depression: February 2007 case

Diana Bou Karam, Cyrille Flamant, Juan Cuesta, Jacques Pelon, Earle Williams

JOURNAL OF GEOPHYSICAL RESEARCH, VOL. 115, D00H27, doi:10.1029/2009JD012390, 2010

Dust emission and transport associated with a Saharan depression: February 2007 case

Diana Bou Karam,[1] Cyrille Flamant,[1] Juan Cuesta,[2] Jacques Pelon,[1] and Earle Williams[3]

Received 30 April 2009; revised 23 October 2009; accepted 22 January 2010; published 15 July 2010.

[1] The dust activity over North Africa associated with the Saharan depression event in February 2007 is investigated by mean of spaceborne observations, ground-based measurements, and mesoscale simulation with Meso-NH. The main characteristics of the cyclone as well as the meteorological conditions during this event are described using the European Centre for Medium-Range Weather Forecasts (ECMWF). The dust storm and cloud cover over North Africa is thoroughly described combining for the first time Spinning Enhanced Visible and Infra-Red Imager (SEVIRI) images for the spatiotemporal evolution and Cloud-Aerosol Lidar and Infrared Pathfinder Satellite Observation (CALIPSO) and CloudSat observations for the vertical distribution. The Saharan depression formed over Algeria in the lee of the Atlas Mountains on the afternoon of 20 February in response to midlatitude trough intrusion. It migrated eastward with a speed of 11 m s^{-1} and reached Libya on 22 February before exiting the African continent toward the Mediterranean Sea on 23 February. The horizontal scale of the cyclone at the surface varied between 800 and 1000 km during its lifetime. On the vertical the cyclone extended over 8 km, and a potential vorticity of 2 potential vorticity units (PVU) was reported at its center at 3 km in altitude. The cyclone was characterized by a surface pressure anomaly of about 9 hPa with respect to the environment, a warm front typified at the surface by an increase in surface temperature of 5°C, and a sharp cold front characterized by a drop in surface temperature of 8°C and an increase in 10 m wind speed of 15 m s^{-1}. The cyclone provided dynamical forcing that led to strong near-surface winds and produced a major dust storm over North Africa. The dust was transported all around the cyclone leaving a clear eye at its center and was accompanied by a deep cloud band along the northwestern edge of the cyclone. On the vertical, slanted dust layers were consistently observed during the event over North Africa. Furthermore, the dust was lofted to altitudes as high as 7 km, becoming subject to long-range transport. The model was able to reasonably reproduce the structure, lifetime, and trajectory of the cyclone. Also, comparison with Moderate Resolution Imaging Spectrometer (MODIS) deep blue aerosol optical depths and CALIPSO-CloudSat observations suggests that the model can be reliably used to quantify the dust emissions associated with this event. The mean daily dust loads over the area influenced by the cyclone were simulated to range between 2 and 8 Tg during the lifetime of the Sharav cyclone (i.e., 5 days). This study suggests that dust emissions linked with Saharan cyclones may contribute significantly to the total dust load over West and North Africa observed annually.

Citation: Bou Karam, D., C. Flamant, J. Cuesta, J. Pelon, and E. Williams (2010), Dust emission and transport associated with a Saharan depression: February 2007 case, *J. Geophys. Res.*, *115*, D00H27, doi:10.1029/2009JD012390.

1. Introduction

[2] Airborne mineral dust is an important component of the Earth's climate system by virtue of its important but poorly quantified influence on the Earth's radiation budget [e.g., *Intergovernmental Panel on Climate Change*, 2001]. A key requirement for the understanding of the effects of mineral dust on the climate system is that an adequate description of the meteorological processes controlling dust emission and transport from source areas be achieved.

[1] LATMOS, IPSL, Université Pierre et Marie Curie, CNRS, Paris, France.
[2] LMD, IPSL, Ecole Polytechnique, CNRS, Palaiseau, France.
[3] Parsons Laboratory, Massachusetts Institute of Technology, Cambridge, Massachusetts, USA.

0148-0227/10/2009JD012390

[3] North Africa is the world's most important dust source area [e.g., *Prospero et al.*, 2002]; providing an estimated dust production of 50% of the global annual total [*Engelstaedter et al.*, 2006; *Laurent et al.*, 2008].

[4] For Saharan dust emission, numerous atmospheric processes on synoptic, regional and local scales provide the meteorological conditions suitable for dust mobilization over areas rich in deflatable sediments (i.e., mountain foothills where fluvial sediment provides erodible materials [e.g., *Péwé*, 1981]). Dust storms have been documented to be associated with high near-surface wind speeds resulting from the downward mixing of momentum from the nocturnal low-level jets (LLJs) [e.g., *Washington and Todd*, 2005; *Todd et al.*, 2008a; *Knippertz*, 2008; *Schepanski et al.*, 2009]. Dust emission over the Sahara has also been shown to be connected with the low-level dynamics associated with the penetration of an upper level trough to low latitudes [e.g., *Jankowiak and Tanré*, 1992; *Knippertz and Fink*, 2006; *Tulet et al.*, 2008; *Cavazos et al.*, 2009], or to density currents caused by strong evaporational cooling along precipitating cloud bands over the northern Sahara [*Knippertz and Fink*, 2006] and along the Sahara side of the Atlas Mountain chain in southern Morocco [*Knippertz et al.*, 2007].

[5] Furthermore, heavy dust storms over North Africa, especially in winter and spring time, have been reported to be associated with Saharan depressions or Sharav cyclones [*Lee*, 1983; *Westphal et al.*, 1985; *Alpert and Ziv*, 1989; *Schepanski et al.*, 2009]. The development of these Saharan depressions, mostly in the lee of the Atlas Mountains, is favored by the strengthening of the meridional temperature gradient over northern Africa in this time of the year. They frequently bring strong winds and sandstorms [*Alpert and Ziv*, 1989], with dust transported over long distances, affecting the Mediterranean Basin [*Moulin et al.*, 1998]. *Barkan et al.* [2005] have noted that the most Saharan dust transport toward Europe occurs in spring and is caused by intense cyclones traveling eastward that pass the North African coast of the Mediterranean. The northward transport of dust is ensured by the strong southwestern flow along the eastern flank of the cyclone [e.g., *Prodi and Fea*, 1979].

[6] Although Saharan cyclones are important synoptic features for dust activity over North Africa that have an influence at scales far beyond the regional one, very few studies of dust mobilization by Saharan depressions have been made and most of them were based on local observations of visibility rates [e.g., *Bartholy et al.*, 2008; *Erel et al.*, 2006].

[7] The purpose of this paper is twofold: (1) to examine, using satellites observations with high spatiotemporal resolution, dust emission and transport over North Africa in connection with the Saharan cyclogenesis event of February 2007; and (2) to estimate dust emissions associated with this event through a numerical study. It is structured as follows: Section 2 provides an overview of the main characteristics of the Saharan cyclones. In section 3 the numerical simulation and the data sources used in this study are described. Section 4 details the meteorological conditions accompanying the cyclogenesis event. The main characteristics of the cyclone under scrutiny are described in section 5. The spatiotemporal evolution of the dust storm is discussed in section 6. In section 7, the dust loads associated with the cyclone are quantified.

2. Overview on Saharan Cyclone Characteristics

[8] Saharan cyclones, sometimes also called Sharav cyclones, Saharan depressions or Khamsin depressions are important synoptic features that occur over North Africa during the winter and spring when the temperature contrast between the North African continent and the Mediterranean Sea is strongest due to the considerable increase in temperatures over the continent relative to the yet cold sea [e.g., *Winstanley* 1970; *Pedgley*, 1972]. Deep north-south oriented troughs in the upper layers of the atmosphere transport cold air from the high latitudes into North Africa. Along the front between this cold air and the warm African air, deep lows form. Often, these lows are associated with hot and sandy southerly winds [e.g., *Egger et al.*, 1995]. Low-latitude cyclogenesis events in the North African region also sometimes result in severe and often strong rainfall [e.g., *Lee et al.* 1988] causing flooding and severe disruption to agriculture.

[9] The Saharan depressions are the most frequent type of Mediterranean cyclones [*Trigo et al.*, 1999] and are initiated usually in the leeward side (i.e., east and south) of the Atlas Mountains as the result of the presence of an upper level trough to the west. Previous studies [e.g., *Elfandy*, 1940; *Pedgley*, 1972; *Tantawy*, 1964; *Alpert and Ziv*, 1989; *Alpert et al.*, 1990; *Prezerakos et al.*, 1990; *Dayan et al.*, 1991; *Barkan et al.*, 2005; *Horvath et al.*, 2006] have pointed out the role of at least four mechanisms for the occurrence of these depressions over North Africa: (1) Large-scale weak baroclinity, (2) vigorous boundary layer baroclinity (due to the strong meridional temperature gradient along the northern African coast), (3) subtropical jet stream related circulations, and (4) lee effects of the mountains.

[10] *Elfandy* [1940]; *Tantawy* [1964]; *Reiter* [1975]; *Alpert and Ziv* [1989] and *Trigo et al.* [2002] have described the Saharan cyclones to be characterized by

[11] 1. An active warm front to the east and northeast of the pressure low associated with high surface temperatures (an increase in surface temperature of 7–8°C is commonly observed).

[12] 2. A cold front to the west and southwest of the pressure low well defined at the surface and often characterized by a drop in surface temperatures of 10–20°C, a shallow cold air mass (1–2 km), and shallow clouds nonprecipitating in general.

[13] 3. The Saharan cyclones move eastward mostly following the North African coast faster than 10 m s^{-1}, and their speed variability during their lifetime (2 to 4 days) is quite low.

[14] 4. The Saharan depressions are associated with a low pressure at the surface of approximately 10 hPa which is reached by nearly 90% of these depressions at 1800 Universal Coordinated Time (UTC). The behavior of the Saharan cyclones is modulated by the diurnal forcing; they exhibit a pronounced diurnal cycle with the triggering and mature stages mostly reached by late afternoon or early nighttime, while cyclolysis tends to occur in early morning.

[15] 5. The Saharan lows represent a near-surface diameter on the order of 500–1000 km. They are located in the lower troposphere with a vertical extent of 3–5 km.

[16] 6. Finally, the occurrence of the Saharan cyclones is typified by heavy sand and dust storms. Around the cyclone the tangential wind is very strong (>10 m s^{-1}) and the vertical flow related to the convective forces is also of considerable strength. The joint effect of these two flows causes uplifting of the dust to high altitudes (500 hPa and above) and its transport over long distances.

3. Data Sources

3.1. Spaceborne Observations

[17] Satellites observations at high spatiotemporal resolution are used in this study in order to characterize qualitatively (using MSG-SEVIRI and Cloud-Aerosol Lidar and Infrared Pathfinder Satellite Observation (CALIPSO)-CloudSat) and quantitatively (using Moderate Resolution Imaging Spectrometer (MODIS) and OMI) the dust activity over North Africa associated with the Saharan cyclone.

[18] The horizontal distribution of dust is described using the SEVIRI images of the Meteosat Second Generation (MSG) computed from a combination of three infrared channels, namely channel 10 (12 μm), channel 9 (10.8 μm) and channel 7 (8.7 μm). MSG-SEVIRI is located geostationary at 0°W over the equator and provides images of Africa on a 15 min temporal resolution. False-color images are created using an algorithm developed by EUMETSAT which colors red the difference between the 12.0 and 10.8 μm channels, green the difference between the 10.8 and 8.7 μm channels and blue the 10.8 μm channel [e.g., *Schepanski et al.*, 2007]. On these composite images, dust appears pink or magenta and cloud appear orange or brown. Note that the dust effect on brightness temperature differences depends on its altitude [e.g., *Pierangelo et al.*, 2004] suggesting that these composite images may favor the dust which is elevated so that its radiating temperature differs significantly from the ground.

[19] Additionally, the aerosol optical depth (AOD) fields obtained from the Moderate Resolution Imaging Spectroradiometer (MODIS)/AQUA Deep Blue Collection 5.1 over desertic surfaces (MYD08_D3 product) as well as the daily Aerosol Index (AI) product derived from the Ozone Monitoring Instrument (OMI) with horizontal resolution of 1° × 1° are used to characterize the dust storm. It is worth noting that the OMI AI depends on the height of the dust cloud, OMI AI being more sensitive to higher dust [e.g., *Chiapello et al.*, 1999].

[20] Finally, information about the vertical distribution of dust during the event under scrutiny is provided from attenuated backscatter profiles (or reflectivity profiles) at 532 nm retrieved from the spaceborne Cloud-Aerosol Lidar with Orthogonal Polarization (CALIOP) on board the CALIPSO [*Winker et al.*, 2003] satellite with vertical and horizontal resolutions of 60 m and 12 km, respectively. The CALIOP-derived reflectivity at 532 nm is used as a proxy to describe the dust layer structure over the Sahara [e.g., *Fan et al.*, 2004; *Flamant et al.*, 2007; *Cuesta et al.*, 2008], as it depends on dust concentration and optical properties. The type and structure of the clouds that formed during the cyclogenesis event is identified using CloudSat observations [*Stephens et al.*, 2008]. It is worth noting that all the instruments/platforms are part of the A-Train except for MSG. The A-Train orbit overpasses North Africa twice a day, once during the daytime (between 1230 and 1430 UTC) and once during the nighttime (between 0030 and 0230 UTC), and has a revisit time period of the same orbit of 16 days [*Stephens et al.*, 2002].

3.2. Ground-Based Measurements

[21] Surface thermodynamics measurements are also used to describe the meteorological conditions accompanying the cyclone development and migration. Surface wind (10 m above ground level (agl)), temperature (2 m agl), pressure and visibility were obtained from meteorological station instruments deployed at Tindouf (Algeria; 27.68°N, 8.15°W), Adrar (Algeria; 27.8°N, 0.18°W), Hassi (Algeria; 31.7°N, 6.0°E), Tripoli (Libya; 32.88°N, 13.17°E), Benina (Libya; 32°N, 20°E,) and Alexandria (Egypt; 31.20°N, 29.95°E; see Figure 2). These data were supplied by the Department of Atmospheric Sciences at the University of Wyoming.

3.3. Model Data

3.3.1. ECMWF Analysis

[22] Synoptic-scale meteorological conditions during the event under scrutiny were established using 6 hourly European Centre for Medium-Range Weather Forecasts (ECMWF) analyses at 925 and 300 hPa of horizontal winds and potential temperature with a horizontal resolution of 0.5°. Additionally, ECMWF analyses of mean sea level pressure, vertical velocity and potential vorticity at 3 and 7 km were used to characterize the cyclone and describe its evolution. Over the Sahara, the quality of the ECMWF analyses is likely to be worse due to the paucity of synoptic stations and radiosondes data [e.g., *Knippertz et al.*, 2009]. The ECMWF analyses in this region are mainly dominated by model physics and assimilated satellite data [e.g., *Cuesta et al.*, 2009b].

3.3.2. Mesoscale Simulation

[23] The simulation has been carried out using Meso-NH [*Lafore et al.*, 1998], a nonhydrostatic mesoscale atmospheric model with an online dust emission and transport module [*Grini et al.*, 2006]. The performances of Meso-NH (especially in terms of dynamics, the main factors that drives dust mobilization) are well established and its ability to simulate dust emission and transport over North and West Africa has been highlighted in several recent studies [e.g., *Chaboureau et al.*, 2007; *Tulet et al.*, 2008; *Crumeyrolle et al.*, 2008; *Todd et al.*, 2008b; *Bou Karam et al.*, 2009a; *Bou Karam et al.*, 2009b].

[24] The parameterizations of deep convection [*Bechtold et al.*, 2001] and cloud microphysics [*Cohard and Pinty*, 2000] included in Meso-NH were activated in order to take into account the formation of clouds associated with the cyclone. Meso-NH is coupled to an externalized surface model, the Soil Biosphere and Atmosphere model (ISBA) [*Noilhan and Mahfouf*, 1996] which handles interactions between the low-level atmosphere and natural land surfaces. The dust emission scheme is the Dust Entrainment And Deposition (DEAD) model [*Zender et al.*, 2003], implemented as a component of Meso-NH [*Grini et al.*, 2006], that calculates dust flux from wind friction velocity. DEAD includes entrainment thresholds for saltation, moisture inhibition and saltation feedback.

[25] The ORILAM model [*Tulet et al.*, 2005] simulates transport and loss processes by following the evolution of

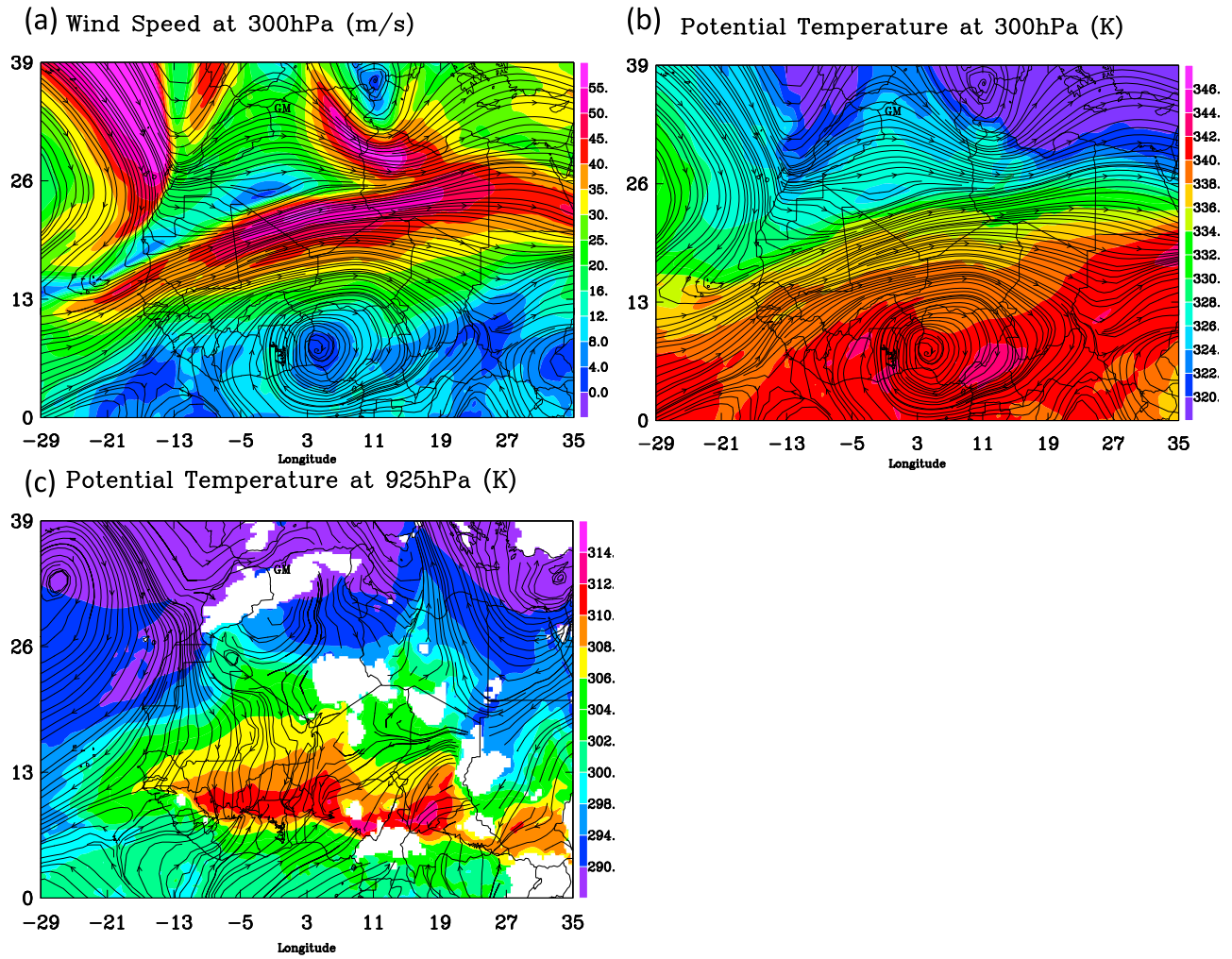

Figure 1. ECMWF analyses on 20 February 2007 at 0000 UTC of (a) wind speed (colors) and direction (streamlines) at 300 hPa and (b) potential temperature (colors) and wind direction (streamlines) at 300 hPa. (c) Same as Figure 1b, but at 925 hPa.

two moments of three lognormal modes defined by *Alfaro and Gomes* [2001]. Dust advection and diffusion are quantified by the transport processes and methods used in Meso-NH which include mixing within the planetary boundary layer, shallow convective transport and advection by winds. The dust loss processes in aqueous phase are not taken into account. Meso-NH uses the radiative scheme of the European Centre for Medium-Range Weather Forecasts (ECMWF), which computes shortwave and longwave radiative fluxes. Shortwave radiative fluxes are computed for 6 wavelengths using the extinction coefficients, asymmetry factors and single scattering albedo provided by look-up tables.

[26] In this study a 6 day simulation (20–25 February 2007) was performed. The study area covering North Africa and the Mediterranean Sea forms a domain of 2500 × 2500 km (centered on 30°N/7°E) with a horizontal mesh size of 25 km. In the vertical, 72 levels were used with 35 of them within the planetary boundary layer (i.e., below 2 km). The lowermost level is at 10 m above the ground, while the highest level is at 28 km above the ground. Initial and lateral boundary conditions were taken from the ECMWF analyses.

4. Meteorological Conditions Before the Cyclogenesis Event

[27] As demonstrated in previous studies, North African cyclogenesis results from the combination of at least three factors. In addition to the orographic forcing that affects the nature of the cyclogenesis [e.g., *Hare* 1943; *Egger et al.*, 1995; *Horvath et al.*, 2006], interactions between the upper level troposphere structure and the low-level baroclinity offer the optimal conditions to trigger the growth of the Saharan lows [e.g., *Thorncroft and Flocas*, 1997; *Trigo et al.*, 2002].

4.1. Upper Level Jets

[28] The situation at the upper levels of the troposphere (i.e., 300 hPa) before the initiation of the cyclogenesis (i.e., before 20 February at 1600 UTC) is described using the ECMWF analyses for wind speed and direction as well as potential temperature (Figure 1). In the wind field at

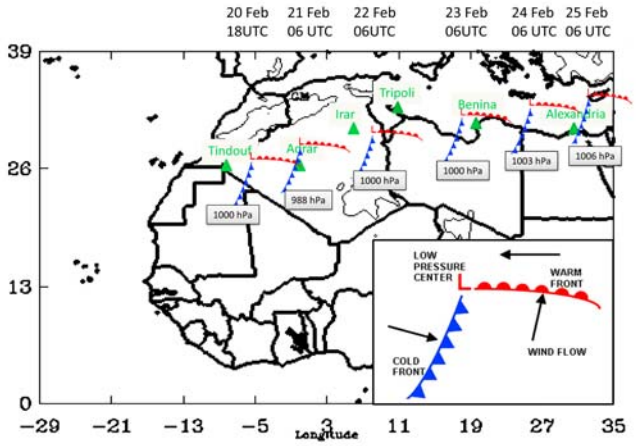

Figure 2. A summary of the spatiotemporal evolution of the cyclone over North Africa between 20 February 2007 at 1800 UTC and 25 February 2007 at 0600 UTC based on the ECMWF analyses for Mean Sea Level Pressure. The pressure at the center of the cyclone is indicated on the gray boxes. The location of the ground stations used in this study is indicated in green.

300 hPa, the Subtropical Jet (STJ) stands out clearly at around 28°N/21°W with strong winds exceeding 55 m s^{-1} (Figure 1a). The zonal component of the STJ was apparent as a core of southwesterly strong winds (in excess of 55 m s^{-1}) reaching 17°N (Figure 1a). Strong winds are also observed at this altitude over northeastern Algeria and western Libya in connection with a depression located over the Mediterranean Sea (38°N/11°E, Figure 1a). The strongest winds are located in the regions of strong potential temperature gradient (Figure 1b). At 300 hPa, in the region of the STJ a well-marked potential temperature gradient of about 7 K over 1000 km can be seen around 21°W (Figure 1b). Furthermore, Nigeria and Benin (close to 3°E and 10°N) were under the influence of a pronounced anticyclone as evidenced by the wind field at 300 hPa (Figure 1a and 1b).

4.2. Low-Level Temperature Gradient

[29] Figure 1c shows the potential temperature and streamlines at 925 hPa on 20 February at 0000 UTC over Africa. A broad baroclinic zone characterized by a temperature gradient of about 8 K over 1000 km (potential temperature values of about 310 K at 12°N and about 290 K at 34°N) is present below the STJ. The maximum of potential temperature (314 K) is located over the continent farther south along a zonal band between 7 and 10°N (Figure 1c). This maximum is associated with daytime surface heating and low pressure and corresponds to the West African heat trough [e.g., *Hastenrath*, 1991]. The minimum of potential temperature (290 K) is located over the Mediterranean Sea and the eastern Atlantic (Figure 1c). The negative meridional gradient of potential temperature seen at low levels (Figure 1c) and at high levels (Figure 1b) satisfies the necessary conditions for baroclinic instability [e.g., *Thorncroft and Flocas*, 1997]; an important precursor for Saharan cyclogenesis [e.g., *Alpert and Ziv*, 1989].

[30] These conditions, qualified as optimal for Saharan cyclogenesis [e.g., *Trigo et al.*, 2002], triggered a Saharan low on 20 February 2007 in the lee of the Atlas Mountains close to 27°N/5°W (see section 5). The cyclone developed at low levels within the region of strong baroclinity and in the presence of an upper level trough perturbed by the orography.

5. Cyclone Characteristics and Evolution Between 20 and 25 February 2007

[31] Based on the ECMWF analyses of mean sea level (msl) pressure and winds at 925 hPa, the spatiotemporal evolution of the cyclone over North Africa during the event under scrutiny was summarized in Figure 2. The cyclone was present over the North African continent during a 4 day period (Figure 2); after being initiated on 20 February around 1600 UTC over western Algeria close to southeast of the Atlas Mountains, it deepened during the following 3 days as it moved eastward. The depression started weakening on 24 February at 0600 UTC, became a shallow depression on 25 February over the eastern coast of the Mediterranean Sea and was no longer seen on 26 February at 0600 UTC.

[32] During its lifetime, the depression was marked by a surface pressure anomaly of about 9 hPa with respect to the environment and seemed not to be influenced by the diurnal forcing except on 22 February when it weakened at 1200 UTC and strengthened from midnight on (not shown). The center of the cyclone remained over the continent from 20 February until 23 February at 0000 UTC when it exited the continent for the Mediterranean Sea in the Gulf of Libya (Figure 2). The Saharan depression moved eastward with a speed of 11 m s^{-1} and northward with a speed of ~2 m s^{-1} on average over the 4 days (Figure 2). The eastward displacement speed was steady during the whole period. The diameter of the cyclone (as delineated from values of mean sea level pressure less than 1005 hPa and closed circulation in the wind field at 925 hPa) was found to be on the order of 800 km over the period with the largest diameter (~1000 km) on 21 February at 1200 UTC (not shown). In the vertical, the cyclone extended over 8 km as inferred by the presence of closed circulation in the wind field at different levels below 8 km.

[33] The cyclone was associated with a cold frontal structure southwest of the pressure low that reached as far south as 15°N and was characterized by potential temperature values at 925 hPa less than 292 K (Figure 3a). On 21 February the temperature gradient at 925 hPa across the cyclone cold front was evaluated to be about 8 K over 100 km (Figure 3a). Advection of warm air (~ 306 K) east of the pressure low (centered at 26°N/0°E) can also be seen in the potential temperature field at 925 hPa (Figure 3a). A vertical cross section at 0°E through the cyclone on 21 February at 0600 UTC (Figure 3b) shows strong ascent (in excess of 0.20 m s^{-1}) near 29°N over a depth of 8 km and large subsidence (−0.1 m s^{-1}) close to 25°N over a depth of 6 km.

[34] The potential vorticity at the center of the cyclone during its lifetime was evaluated to be as large as 2 potential vorticity units (PVU) below 6 km above mean sea level (msl) (Figure 3c). At 7 km msl the potential vorticity reached 4 PVU (Figure 3d). Large values of potential vorticity (2–4 PVU) were also seen along the southern edge of the

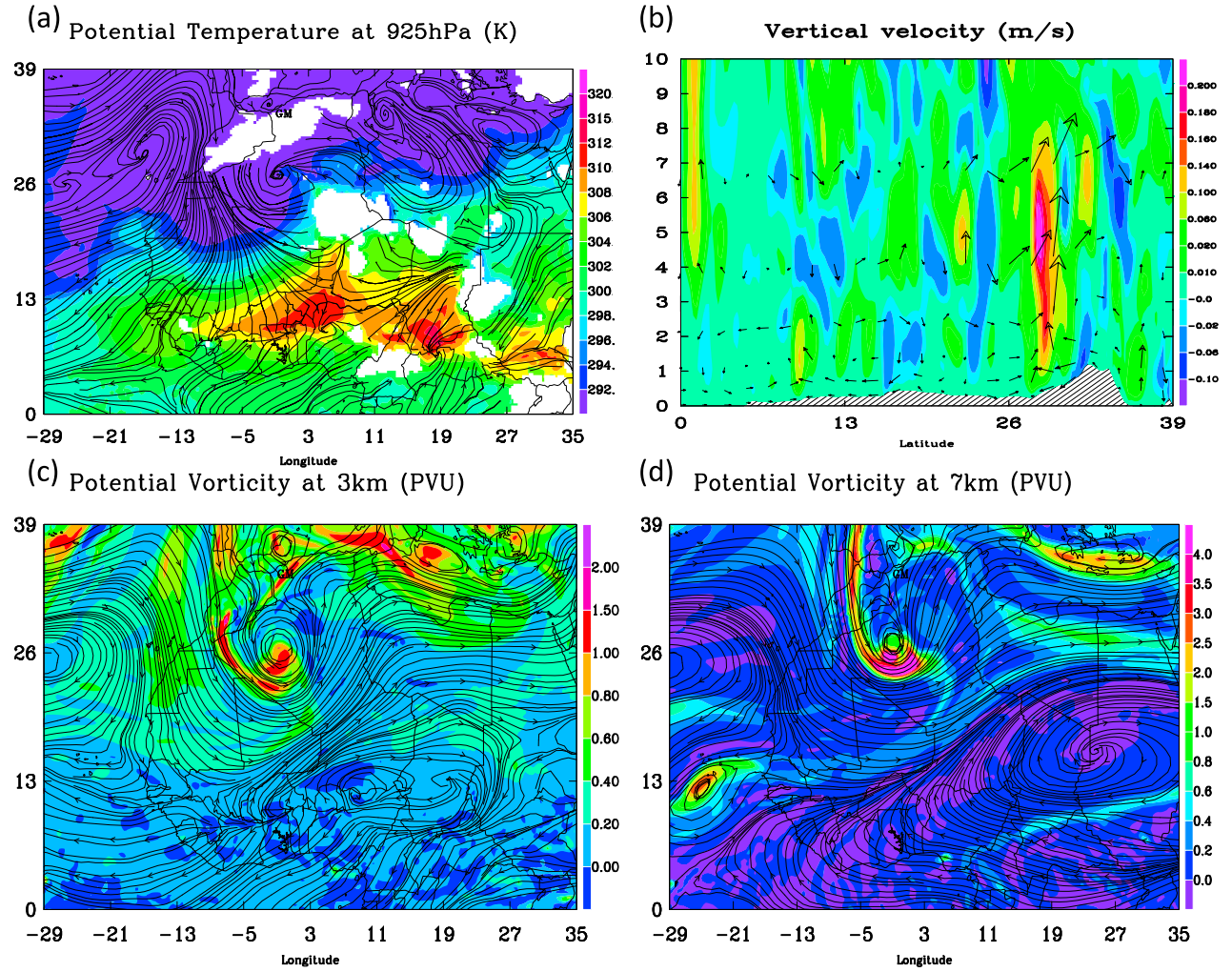

Figure 3. ECMWF analyses on 21 February 2007 at 0600 UTC of (a) potential temperature (colors) and wind direction (streamlines) at 925 hPa. The black line represents the location of the cross section at 0°E. (b) Vertical velocity (colors) and wind direction (arrows) along the black line shown in Figure 3a. (c) Potential vorticity (colors) and wind direction (streamlines) at 3 km. (d) Same as Figure 3c, but at 7 km.

cyclone (close to 24°N) due to the strong shear expected in this area (Figure 3c and 3d). During the cyclolysis (i.e., from 24 February at 1200 UTC) the cyclone was associated with potential vorticity values in its center less than 1 PVU (not shown).

[35] Strong winds were seen around the cyclone during its lifetime with a region of very weak winds (less than 3 m s^{-1}) in its center (e.g., on 21 February at 1200 UTC; see Figure 4a). At 925 hPa, the peak wind speed around the cyclone varied over the 4 days between 20 and 25 m s^{-1} (e.g., on 21 February at 1200 UTC; see Figure 4a). At higher levels (i.e., at 700 hPa) the peak winds accompanying the cyclone were much stronger and varied between 30 and 40 m s^{-1} over the 4 day period (e.g., on 21 February at 1200 UTC; see Figure 4b).

[36] The passage of the cyclone over North Africa was recorded at different meteorological stations. The temporal evolution over the 4 day period of surface temperature (at 2 m agl), pressure, visibility and wind speed (at 10 m agl) at Tindouf, Adrar, Hassi, Tripoli, Benina and Alexandria are used in order to characterize the signature of the cyclone at the surface at different stages.

[37] The initiation stage of the cyclone was documented in Tindouf. On 20 February at 1200 UTC the arrival of a cold front from the Atlantic Ocean was marked by an increase in wind speed of 10 m s^{-1} and a drop in surface temperature of about 5°C as estimated with respect to temperature reached at 1200 UTC on subsequent days (Figure 5b). At 1800 UTC the low-pressure center (less than 1000 hPa) was located at 26°N/5°W (i.e., to the east of Tindouf, Figure 5a) and a local minimum of surface pressure (1007 hPa) was observed there at 1400 UTC (Figure 5b).

[38] During its eastward displacement, the cyclone intersected Adrar on 21 February (Figure 5c); its warm front crossed over at midnight and surface temperature increased by 8°C as estimated with respect to the midnight temperatures observed on subsequent days (Figure 5d). At 0600 UTC a strong drop in surface pressure of 13 hPa was reported followed 6 h later by an increase in surface wind speed of 14 m s^{-1} and a decrease in surface temperature of 6°C with respect to temperatures observed on subsequent days at the same time of the day (Figure 5d). On 22 February at 0600 UTC, strong surface winds of about 15 m s^{-1} associated with the cold front

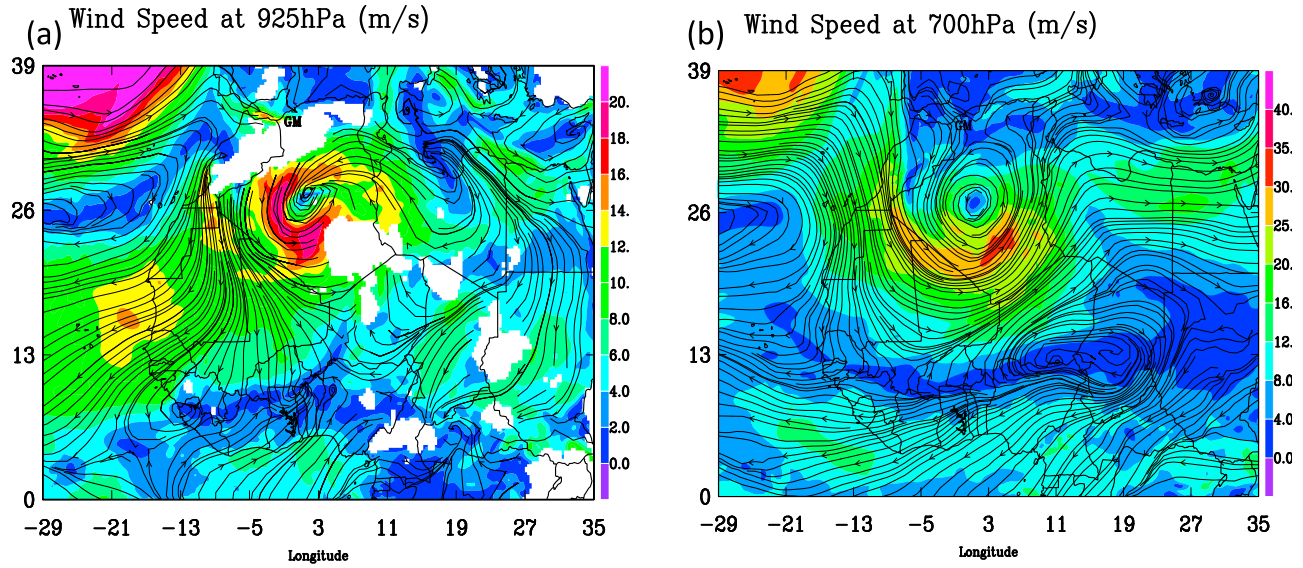

Figure 4. ECMWF analyses of wind speed (colors) and direction (streamlines) at (a) 925 and (b) 700 hPa on 21 February 2007 at 1200 UTC.

of the cyclone (Figure 5e) were observed at Hassi accompanied with a decrease in surface temperature of 5°C and in surface pressure of 8 hPa with respect to the observations on subsequent days (Figure 5f).

[39] The cyclone center passed over Tripoli in the afternoon of 22 February (Figure 6a). A pressure minimum of 1000 hPa was reported in the observations at 1500 UTC accompanied with very weak surface wind speed of about 1 m s^{-1} (Figure 6b). The diurnal cycle of surface temperature was perturbed by the presence of the cyclone over Tripoli; an increase in nighttime surface temperature of 8°C was reported during two consecutive nights on 22 and 23 February with respect to the previous nights. Furthermore, the diurnal cycle in surface temperature was nearly suppressed on 23 February by the passage of the cyclone cold front over Tripoli (Figure 6b).

[40] Before the arrival of the pressure low (1000 hPa) on 23 February between 0600 UTC and 2300 UTC (Figure 6c), the area of Benina was under the influence of the cyclone warm front between 22 February at 1200 UTC and the early morning of 23 February, as inferred from an increase in surface temperature of 10°C in coincidence with an increase in surface wind speed of about 10 m s^{-1} (Figure 6d). The diurnal cycle of surface temperature expressed a similar behavior as in Tripoli with an increase in the nighttime surface temperature (Figure 6d).

[41] On 24 February at 0600 UTC, the cyclone center was over the Mediterranean Sea in front of the Egyptian coast (Figure 6e). Alexandria was under the influence of the cyclone warm front; an increase of 10°C in the nocturnal surface temperatures was reported associated with surface wind speed of about 10 m s^{-1} (Figure 6f).

6. Spatiotemporal Evolution of the Dust Storm

6.1. Horizontal Evolution

[42] An atmosphere heavily laden with dust over North Africa was documented in the SEVIRI images during the Saharan cyclogenesis event (Figure 7). On 20 February, the intrusive cold front from midlatitudes induced strong near-surface winds (up to 25 m s^{-1}) that triggered a dust storm over southern Morocco and western Algeria. Visibility down to 0 km was indicated at Tindouf on 20 February at 1200 UTC (Figure 5b). During the development of the cyclone, dust emission continued to increase, enhanced by strong westerly winds associated with the cold front. By midnight, the cyclone was apparent in the SEVIRI images as a combination of three features; a curved band of clouds on its northern edge located over northern Algeria (close to 30°N), a spiraling band of dust over western Algeria (close to 28°N) accompanied by a large trailing band of dust that reached as far south as 22°N (over Mali and Mauritania) and a dust-free area corresponding to the eye of the cyclone at 27°N (Figure 7a).

[43] As the cyclone moved eastward, strong winds on its south side associated with the cold front continued to mobilize dust over Algeria and northern Mali during the entire day on 21 February (Figure 7b). In addition to the eastward displacement, the dust was transported cyclonically all around the cyclone leaving a clear eye in the center (Figures 7a and 7b). By 21 February at 1800 UTC most of Algeria as well as the western part of Libya were covered by a large cyclonic structure of dust (Figure 7c). Dramatic suppressed visibility conditions (0 km) were reported at Adrar during the whole day on 21 February and till the morning of 22 February (Figure 5d) by which time the cyclone had moved eastward. A sharp drop in visibility associated with the advected dust announced the arrival of the cyclone system over Hassi and values of about 1 km were registered on 21 February at 1200 UTC (6 h before the arrival of the cyclone cold front, Figure 5f).

[44] In the early morning of 22 February, the cyclone reached southern Tunisia and northwestern Libya; it was visible on the SEVIRI images as two nested spiral bands of cloud and dust, the first one was on the side of the cold front and covered the northwestern edge of the cyclone and the second one was on the side of the warm front and covered the southeastern edge of the cyclone (Figure 7d). During the

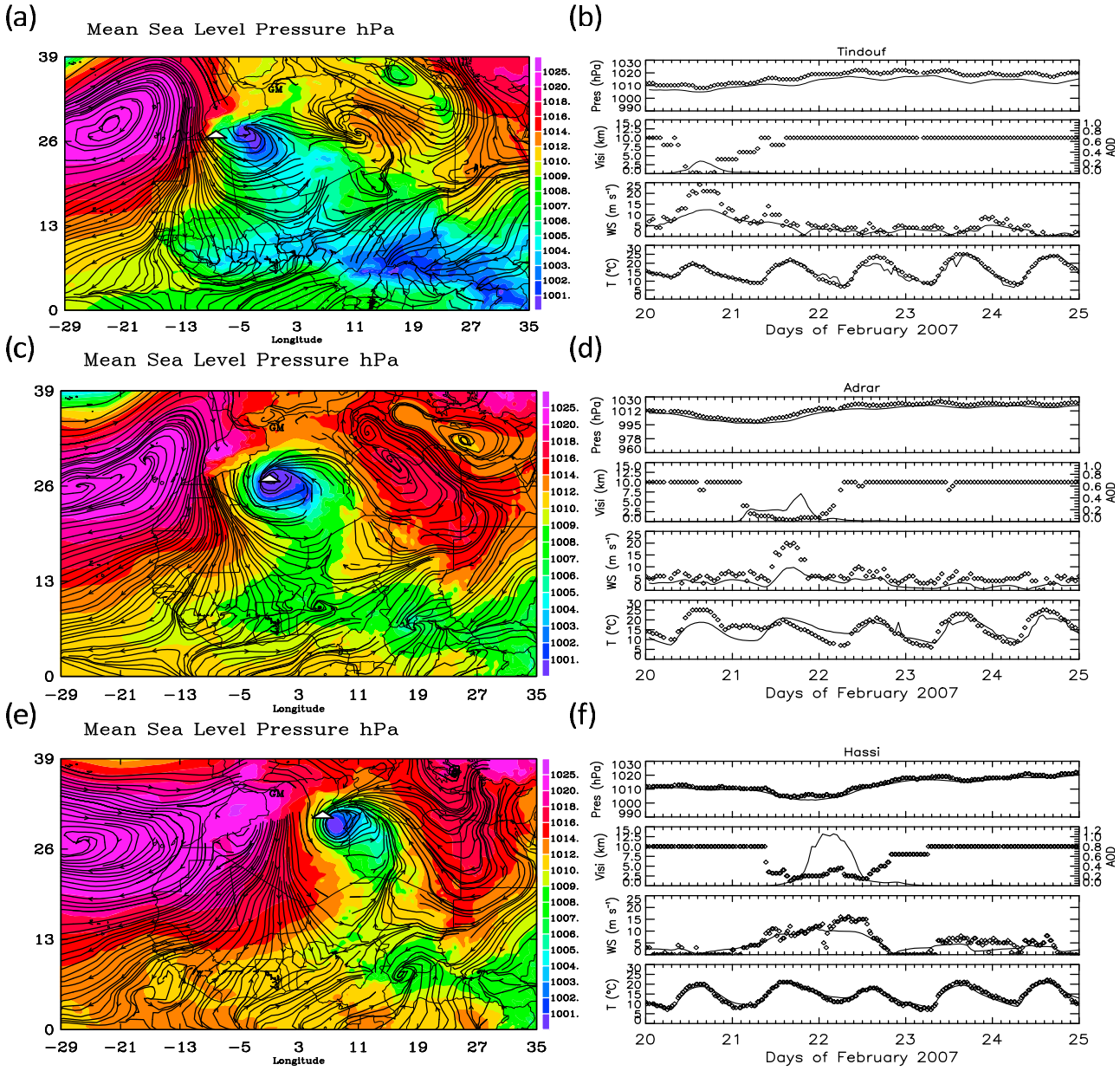

Figure 5. ECMWF analyses of Mean Sea Level Pressure (colors) and wind direction at 925 hPa (streamlines) on (a) 20 February 2007 at 1800 UTC, (c) 21 February 2007 at 0600 UTC, and (e) 22 February 2007 at 0600 UTC. Time series between 20 February 2007 at 0000 UTC and 25 February 2007 at 0000 UTC of surface temperature (at 2 m agl), pressure, visibility, and wind speed (at 10 m agl) at (b) Tindouf, (d) Adrar, and (f) Hassi. The white triangles represent the location of the corresponding ground station. The surface observations are represented by diamonds, and the model data are represented by the black line.

day of 22 February, the cyclone with heavy amounts of dust along its southeastern edge continued to move eastward and northward and visibility started decreasing at Tripoli at noon on 22 February and reached a minimum of 1 km at 1800 UTC (Figure 6b).

[45] By midnight on 23 February, the cyclone left the continent over the Gulf of Libya transporting a heavy cloud of dust toward the Mediterranean Sea (Figure 7e). A drop in visibility to 1.5 km was observed at Benina on 23 February at 1000 UTC (i.e., 10 h after the passage of the cyclone center, Figure 6d). However, strong winds of about 16 m s^{-1} in connection with the cyclone (not shown) continued blowing over eastern Libya and contributed to mobilize large amounts of dust on 23 February (Figure 6e).

[46] In the morning of 24 February, the cyclone center was located over the Mediterranean Sea in front of the Libyan cost and massive dust plumes were transported eastward over the Mediterranean Sea and Egypt (Figure 6f) and reached Lebanon and Israel in the afternoon (Figure 7f). As inferred from the SEVIRI images (not shown), dust emission was

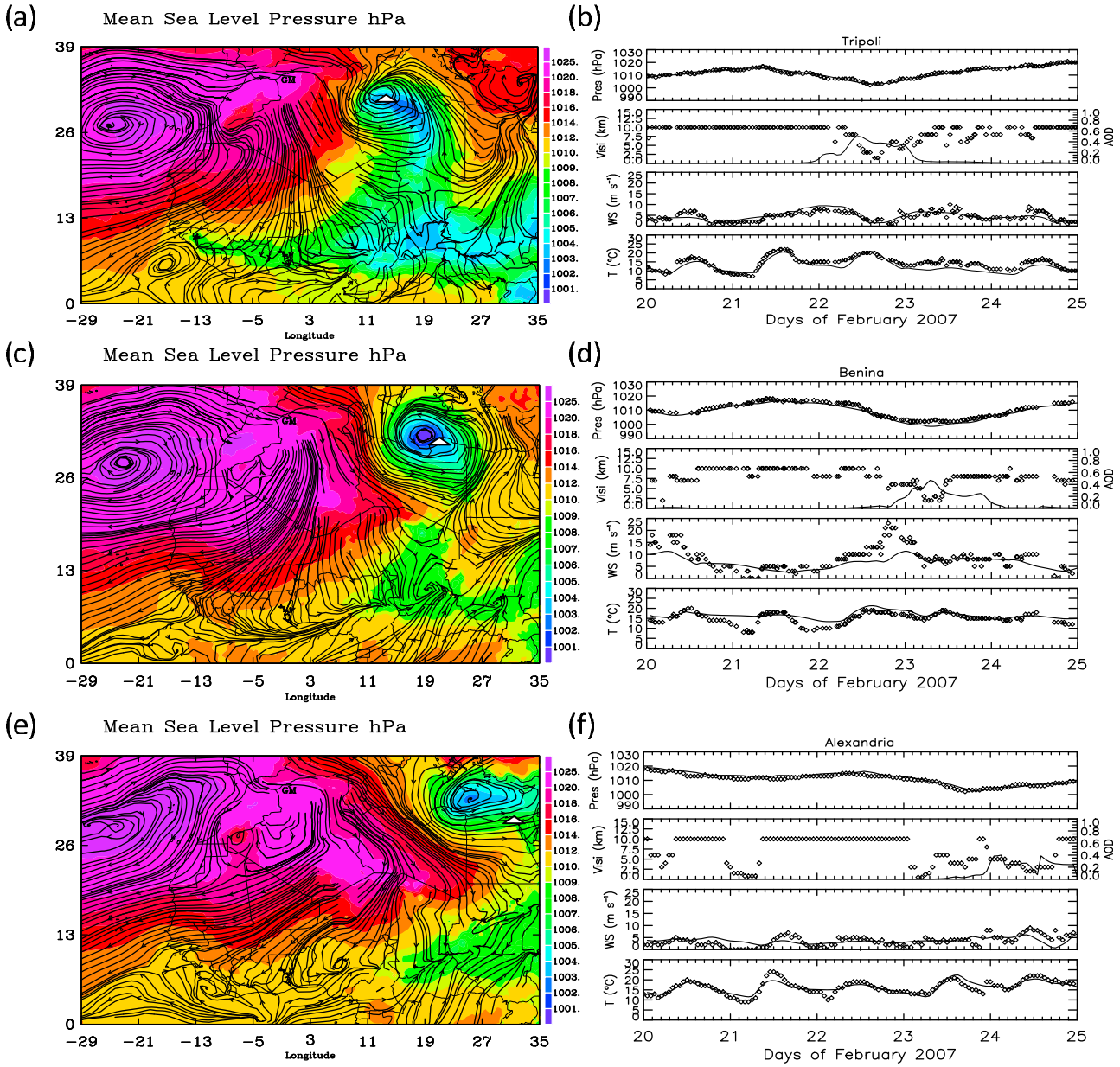

Figure 6. ECMWF analyses of Mean Sea Level Pressure (colors) and wind direction at 925 hPa (streamlines) on (a) 22 February 2007 at 1800 UTC, (c) 23 February 2007 at 0600 UTC, and (e) 24 February 2007 at 0600 UTC. Time series between 20 February 2007 at 0000 UTC and 25 February 2007 at 0000 UTC of surface temperature (at 2 m agl), pressure, visibility, and wind speed (at 10 m agl) at (b) Tripoli, (d) Benina, and (f) Alexandria.

initiated over southern Jordan and northern Saudi Arabia on 25 February when the cyclone center was over Cyprus Island.

[47] The AOD associated with the dust storm under examination was evaluated using the MODIS Deep Blue observations at 550 nm on a daily base resolution (one passage per day around noon time). AOD values of 1.25–1.75 were reported on 21 February (Figure 8a). On 22 February similar AOD values were observed, except around the cyclone center where much higher AODs (on the order of 2.25–2.5) were observed over eastern Algeria and western Libya (Figure 9a). On 23 February, AOD values on the order of 1.5 were seen in the MODIS Deep Blue observations over Libya and Egypt (not shown). MODIS deep blue AODs decreased on 24 February and were on the order of 1.25 over Egypt (not shown). The OMI AI fields on 21 and 22 February showed high values (in excess of 4) all around the eye of the cyclone associated with high dust concentrations (Figures 8b and 9b). At a later stage of the cyclogenesis event (i.e., on 23 and 24 February), the AI was close to 3.5 over the continent and remained on the order of 4.5 over the Mediterranean Sea (not shown).

6.2. Vertical Distribution of Dust and Clouds Over North Africa

[48] The vertical distribution of dust over North Africa during the event is described using CALIPSO for five dif-

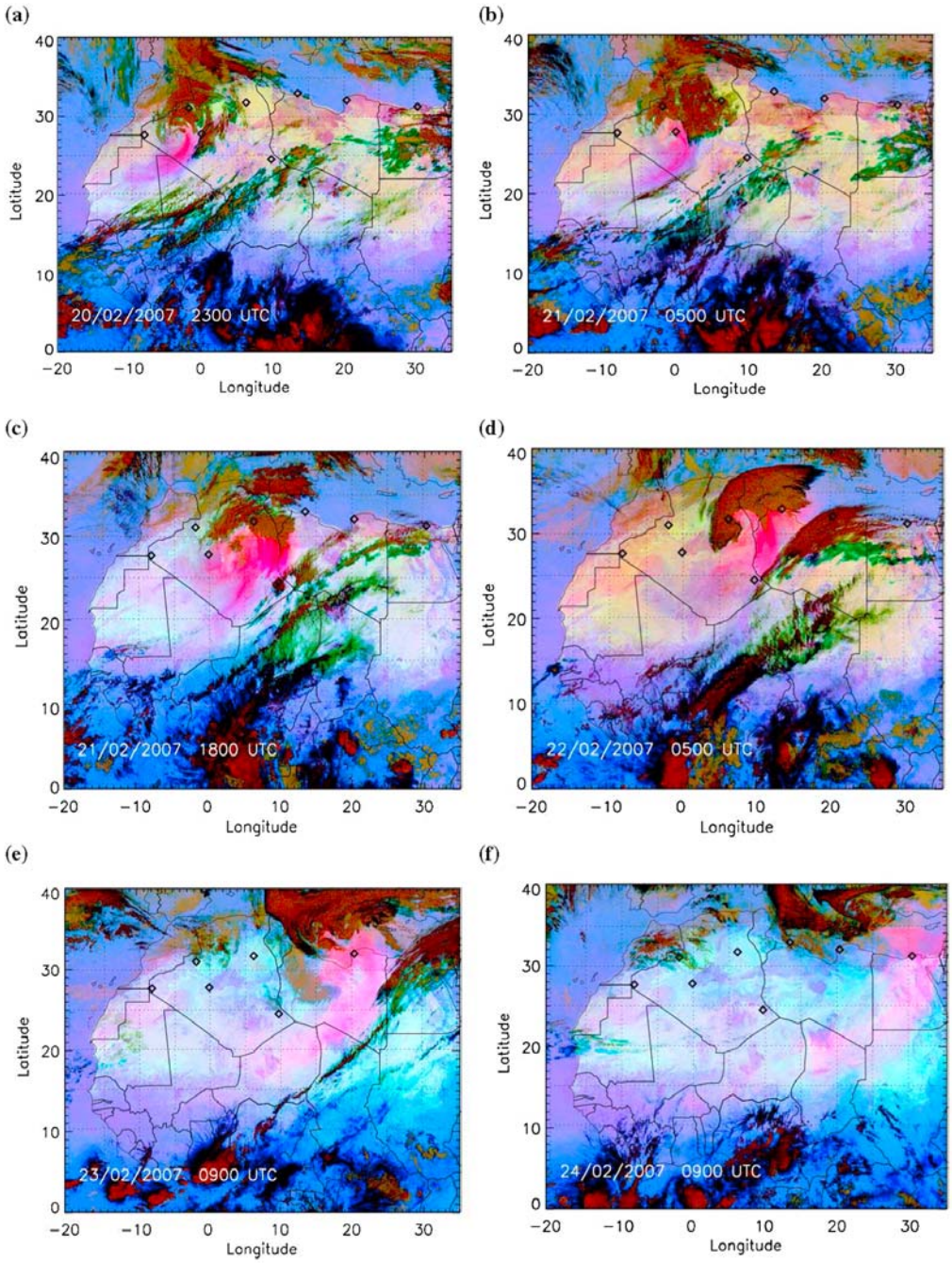

Figure 7. SEVIRI-derived false color images over West Africa, showing dust (pink/purple), clouds (brown/orange), and differences in surface emissivity retrieved in absence of dust or clouds (light blue/blue) on (a) 20 February 2007 at 2300 UTC, (b) 21 February 2007 at 0500 UTC, (c) 21 February 2007 at 1800 UTC, (d) 22 February 2007 at 0500 UTC, (e) 23 February 2007 at 0900 UTC, and (f) 24 February 2007 at 0900 UTC. The black diamonds represent the location of the ground stations.

ferent passages (two through the cyclone and three through the trailing band of dust) over North Africa (Figures 10, 11, and 12). On 22 February at 0200 UTC when the center of the cyclone was located over eastern Algeria (close to 32°N; see Figure 10a), the greater part of southern and eastern Algeria as well as western Libya was covered by a heavy dusty layer (Figure 10a). The CALIOP transect was to the west of the cyclone location and intercepted the dust present over southern Algeria and northern Mali (between 15° and 25°N) which was uplifted previously at the beginning of cyclogenesis (i.e., Figure 7a).

[49] CALIPSO shows large amounts of dust located in the lower troposphere between the ground and 2 km in altitude associated with large reflectivity values in excess of 5.10^{-3} km^{-1} sr^{-1} (Figure 10b). The dust was present within a relatively cold air mass characterized by potential

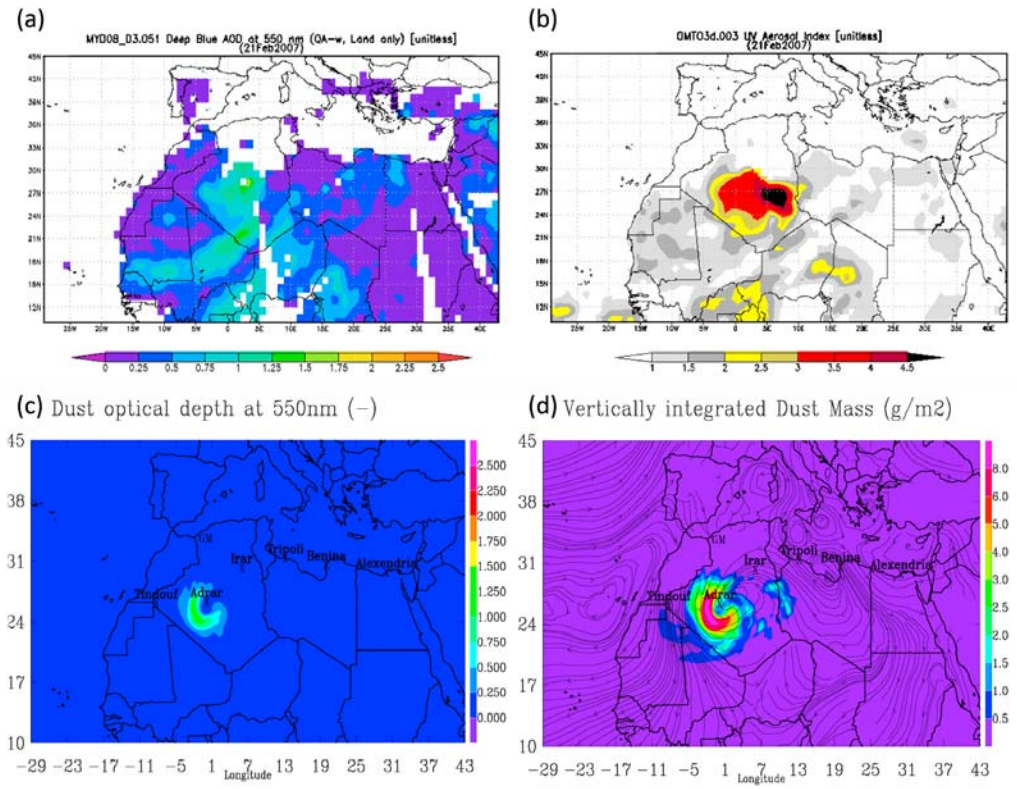

Figure 8. On 21 February 2007 around noon time (a) aerosol optical depth at 550 nm over West Africa (over land) retrieved by the MODIS Deep blue level 2 algorithm (available at http://disc.sci.gsfc.nasa.gov/giovanni/), (b) semiquantitative aerosol index over West Africa retrieved in the ultraviolet by OMI (available at http://toms.gsfc.nasa.gov/), (c) simulated aerosol optical depth at 550 nm, and (d) simulated vertically integrated dust mass (g m^{-2}). The streamlines in Figure 8d represent the wind direction at 925 hPa.

temperature values between 292 K and 300 K (Figure 10b). The nocturnal dusty layer seemed to be well mixed through 2 km in altitude (Figure 10b) probably due to the turbulence associated with the cyclone cold front. To the north of the dust plume, sparse clouds at 8 km msl were seen by CALIOP near 33°N (Figure 10b), corresponding to the western edge of the cyclone-associated cloud cover (Figure 10a).

[50] Ten hours later when the cyclone moved further east over Tunisia and western Libya (Figure 10c), CALIOP passed again to the west of the cyclone. It intercepted this time, in addition to the trailing band of dust, the southwestern part of the cyclone cloud band (Figure 10c). A dusty layer between 18°N and 26°N remained on the CALIPSO transect between the ground and 2 km in altitude (Figure 10d). It corresponds to the dust load over southern Algeria seen in the SEVIRI image (Figure 10c). Furthermore, the cloud band of the cyclone was mostly composed by cold thick high-level clouds (red colors) as well as thick midlevel clouds (brown colors) as can be seen on the SEVIRI images (Figure 10). Additionally, CloudSat observations showed the presence of cirrus (not shown) with a top height of 8 km in altitude (e.g., Figure 10d) suggesting that the cyclone extent in the vertical was comparable with the results obtained from the ECMWF analyses and discussed earlier (Figure 3b). On this daytime CALIPSO passage, the dusty layer was associated with potential temperature below 304 K (Figure 10d). North of the dust plume, a well-mixed layer over 8 km can be seen in the region between 28°N and 33°N (Figure 10d), the closest to the cyclone center (Figure 10c).

[51] At midnight on 23 February, the cyclone center was located over the Mediterranean Sea close to the Libyan coast and its dense cloud band reached as far south as 31°N (Figure 11a). Although the cyclone center was over the Sea, strong winds associated with the cold front provided the dynamical forcing to lift large amounts of dust over northern and central Libya (Figure 11a). High dust load was transported within the northeastern branch of the cyclone over the Mediterranean Sea (close to 33°N; see Figure 11a). At the same time, central Libya, northern Niger and northeastern Chad were covered by a heavy dust layer seen in purple on the SEVIRI image (Figure 11a).

[52] CALIOP intersected the cyclone, through its center, during its nighttime and daytime passages on 23 February (Figures 11b and 12b). During this period, the vertical structure of dust layers south of the cyclone was closely linked to the presence of slanted isentropes (e.g., Figure 11b). After been uplifted and under conditions of near-adiabatic flow, the dust layers were likely to be transported slantwise following the isentropes [e.g., *Cuesta et al.*, 2009a]. Northward winds at the eastern flank of the cyclone (e.g., Figure 6a) were likely to produce a progressive ascent or upgliding [e.g., *Hoskins et al.*, 1985] of the dust layers toward the north. Such

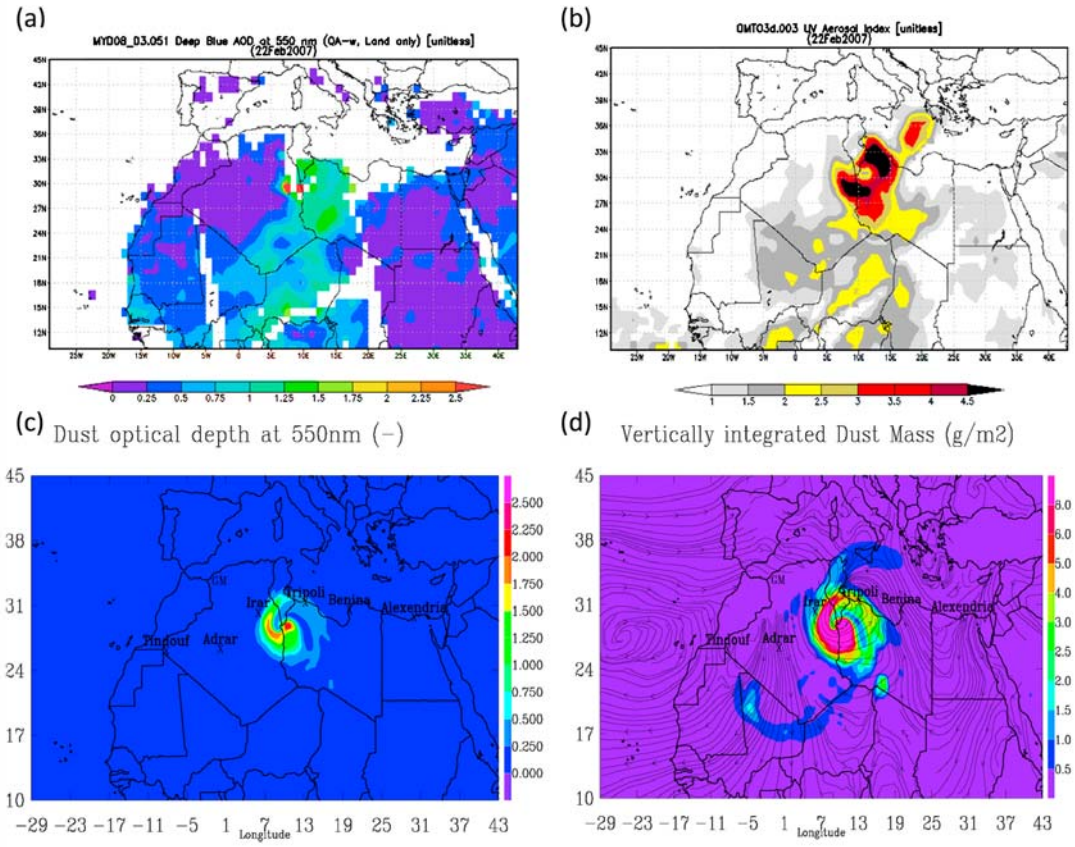

Figure 9. Same as Figure 8, but on 22 February 2007 around noon time.

slanted dust layers were observed by CALIPSO on 23 and 24 February (Figures 11b, 12b, and 12d).

[53] On 23 February (Figure 11b), four 300 m deep dusty layers following the isentropes were seen by CALIPSO in the region south of 20°N. The highest layer was between 2 km (at 15.5°N) and 2.5 km (at 18.5°N) in altitude and was characterized by reflectivity values below 4.10^{-3} km^{-1} sr^{-1} (Figure 11b). The layer below lay between the ground (at 15.5°N) and 2 km (at 19°N) in altitude and was associated with reflectivity values in the same order as the previous layer. Higher dust content (reflectivity values > 5.10^{-3} km^{-1} sr^{-1}) was seen at lower levels in the CALIPSO in connection with two distinct sloping plumes of dust. The southern plume lay between the ground (at 16°N) and 2 km (at 21°N) in altitude, while the northern one extended between the ground (at 18°N) and 1 km (at 20°N).

[54] North of 20°N, in the southbound branch of dust east of the low, a deep dusty layer between the ground (at 20°N) and 2.5 km in altitude (at 24.2°N) was observed on the CALIPSO (with reflectivity > 5.10^{-3} km^{-1} sr^{-1}; see Figure 11b). Further north, a heavy dust layer extended from the ground to 3 km in altitude between 24°N and 29°N. In this region, where strong turbulent mixing associated with the cyclone cold front is expected, vertical mixing of dust across the isentropes was apparent (Figure 11b). Furthermore, a layer of lesser dust content associated with reflectivity values of about 4.10^{-3} km^{1} sr^{-1} was observed between 3 and 7 km in altitude in the region near the cyclone center (i.e., 29°N) where strong upward motion is present (Figures 11b and 3b). This structure of distinct plumes of dust at different latitudes is probably due to the northward displacement of the cyclone and its associated cold front and cyclonic winds. This hypothesis suggests that the further the dusty layer is from the cyclone center, the oldest it is.

[55] The cloud band associated with the cyclone covered a large area between 32°N and 40°N (Figure 11c). The top of the cloud layer increased with latitude; it was at 7 km in altitude at 32°N and reached 10 km at 40°N (Figures 11b and 11c). CloudSat observations indicated the occurrence of deep convection associated with altostratus and altocumulus clouds (Figure 11c).

[56] After 10 h, during its daytime passage on 23 February, CALIOP crossed over the dust storm when it was covering eastern Libya (Figure 12a). An elevated layer of dust was seen in CALIPSO between the 1 and 2.5 km in altitude over the regions located between 22°N and 34°N (Figure 12b). Strong reflectivity (5.10^{-3} km^{-1} sr^{-1}) remained associated with the airborne dust. A deep layer of clouds (9 km in altitude) extended between 34°N and 40°N (Figure 12b) and was associated with deep convection as suggested by CloudSat observations (not shown).

[57] By midnight on 23 February, as the cyclone continued to move eastward over the Mediterranean Sea, the dust front was advected over Egypt and southern Libya (Figure 12c). The dust front was visible in the CALIPSO as a continuous heavy dust layer in the lower troposphere (below 2.5 km),

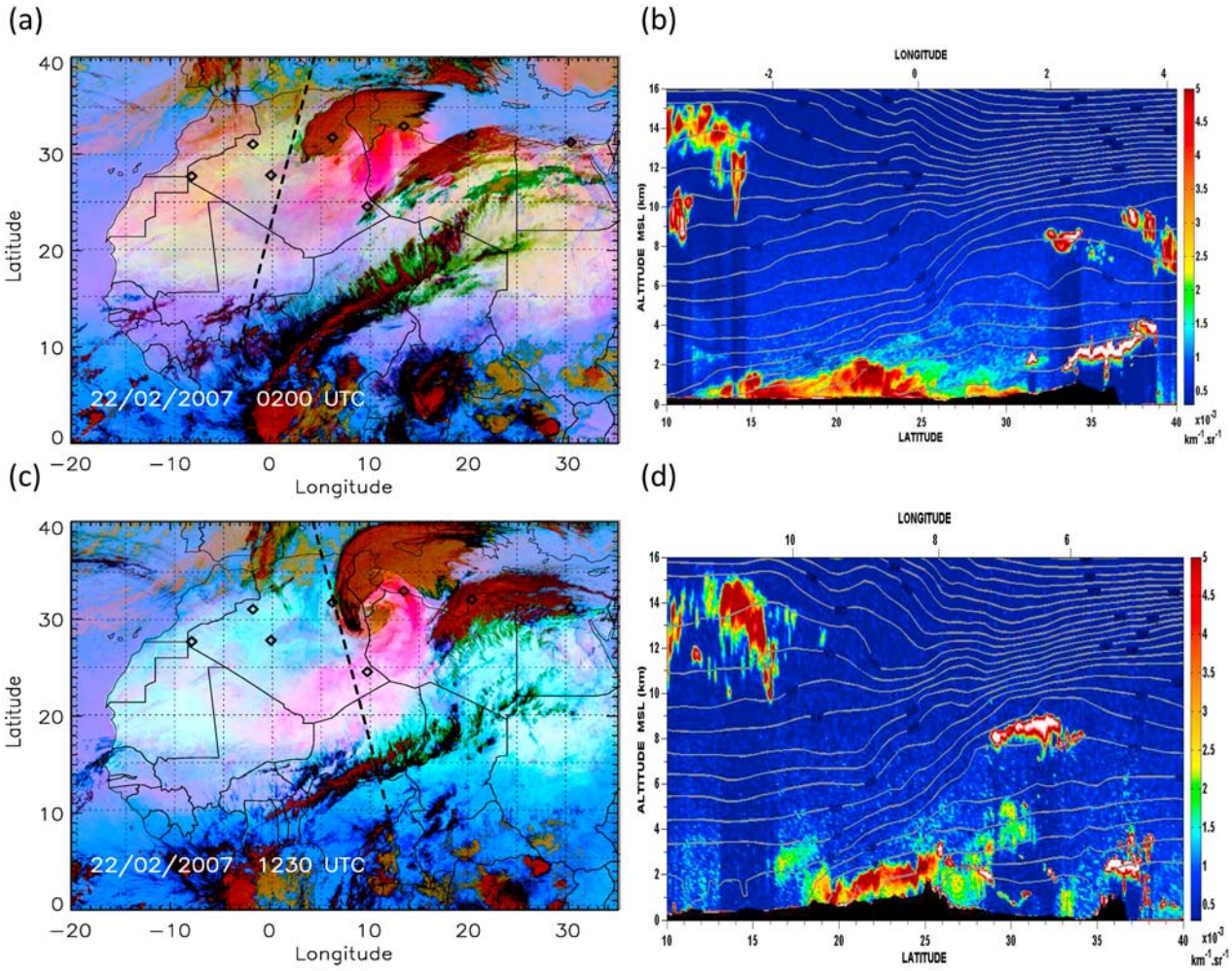

Figure 10. (a) SEVIRI-derived false color images over West Africa on 22 February 2007 at 0200 UTC, showing dust (pink/purple), clouds (brown/orange), and differences in surface emissivity retrieved in absence of dust or clouds (light blue/blue). The dashed black line is the CALIPSO track and the black diamonds are the location of the ground stations. (b) CALIPSO lidar transect over West Africa on the 22 February 2007 at 0201 UTC: attenuated backscatter coefficient profiles at 532 nm (level 1 product available at http://www.icare.univ-lille1.fr/) with a 60 m (12 km) resolution in the vertical (horizontal). The outline of the topography appears in black. Optical thick clouds appear in white; the low backscatter values below them are due to lidar signal extinction. Superimposed on the CALIPSO lidar data are 0000 UTC ECMWF analyses of potential temperature (dark gray plain contours). (c) Same as Figure 10a, but for 1230 UTC. (d) Same as Figure 10b, but for 1255 UTC CALIPSO observations and 1200 UTC ECMWF analysis.

between 22°N and 33°N (Figure 12d). A much elevated dust layer (between 3 and 4 km) was seen over the sea at 35°N corresponding to the dust entrained eastward by the cyclone (Figure 12d). This gain in altitude is probably due to the vertical advection of dust as it passed through the cyclonic system during the eastward displacement.

7. Estimate of Dust Emissions Associated With the Cyclone

7.1. Evaluation of the Simulation Against Observations

[58] The simulation of the Saharan cyclone was evaluated through comparison with surface observations at the different sites (Figures 5 and 6). At Tindouf, the surface pressure was underestimated by the model by as little as 2 hPa (Figure 5b). The observed strong wind speed associated with the arrival of the cold front from high latitudes on 20 February was underestimated by the model by about 15 ms^{-1} (Figure 5b) though the diurnal variation in wind speed was relatively well reproduced for the other days. Furthermore, the reduction in visibility on 20 February due to dust emissions was associated with an increase in the simulated AODs (Figure 5b). Finally, the diurnal cycle of surface temperature was well captured by the model.

[59] On the following day, the model simulated well the variation in surface pressure associated with the arrival of the depression over Adrar (Figure 5d). However, the strong winds associated with the cold front of the cyclone remained

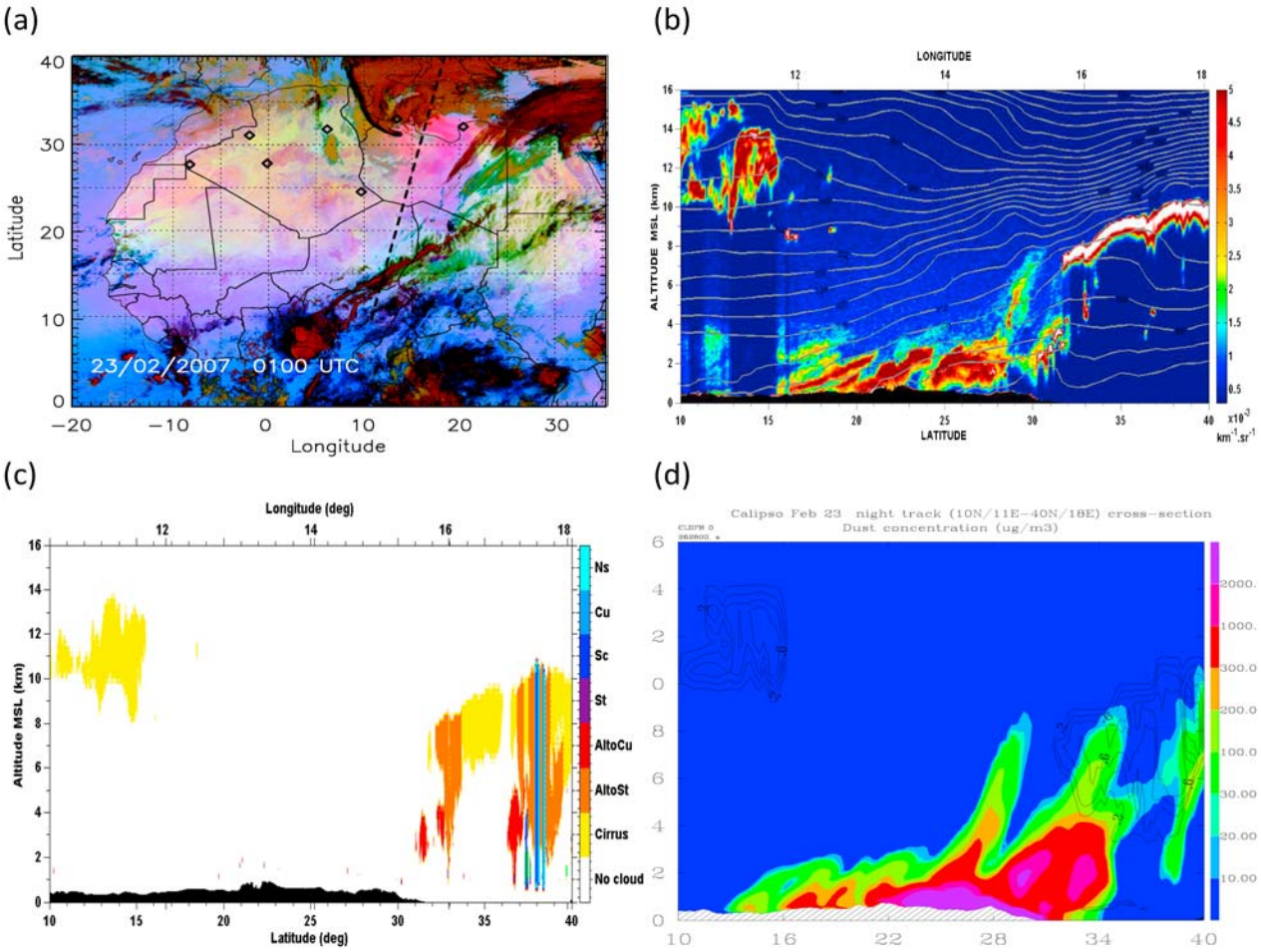

Figure 11. (a) Same as Figure 10a, but for 23 February 2007 at 0100 UTC. (b) Same as Figure 10b, but for 23 February 2007 at 0103 UTC. (c) CloudSat radar transect over West Africa on 23 February 2007 at 0103 UTC (coaligned with CALIPSO lidar) of level 2 cloud type classification in colors (available at http://disc.sci.gsfc.nasa.gov/giovanni/). (d) Simulated dust concentrations (colors) and cloud fraction (isocontours) along CALIPSO track.

underestimated by 10 ms^{-1}. The drop in visibility was associated with an increase of 0.5 in AOD (Figure 5d). At Adrar, the model showed difficulties in producing the diurnal cycle of surface temperature. Comparisons between the model and the observations at Hassi showed a better representativity of the surface pressure, the surface temperature and the wind speed at 10 m agl. The sharp decrease in visibility observed at Hassi was associated with much higher AOD of about 1.2 (Figure 5f). Same behavior was seen at Tripoli (Figure 6b) with simulated AODs on the order of 0.5. At Benina, the maxima in surface wind speed were not captured by the model particularly on 23 February (Figure 6d). Also the minima in surface temperature during night on 20 and 21 February were not reproduced by the model (Figure 6d). At Alexandria, the model simulated well the variation in surface pressure, temperature and wind speeds over the period (Figure 6f). The reduction in visibility at Alexandria was associated with simulated AODs of about 0.3 (Figure 6f). In conclusion, it appears that Meso-NH did reproduce realistically the timing of the event (and hence its northeastward propagation). On the other hand, the strong winds associated with the passage of the cold front (the main driver for the dust uplifts over northern Africa) were found to be undervalued, sometimes substantially. Nevertheless, wind speeds associated with the passage of the cold front were always simulated to be in excess of 10 m s^{-1}, i.e., above the threshold wind speed generally considered to enable soil erosion by eolian processes over the Sahara [e.g., *Fernandez-Partagas et al.*, 1986].

[60] The simulation of the dust activity associated with the Saharan cyclone was evaluated quantitatively through comparisons with the MODIS Deep Blue AODs and qualitatively through comparisons with OMI AI and CALIPSO. On 21 February 2007 at 1200 UTC, the simulated AODs by Meso-NH at 550 nm were of about 1.5 (Figure 8b), i.e., similar to those observed by MODIS Deep Blue to be on the order of 1.75 (Figure 8a). However, the area of high AODs simulated by Meso-NH was smaller and more localized than the area of same AODs observed by MODIS.

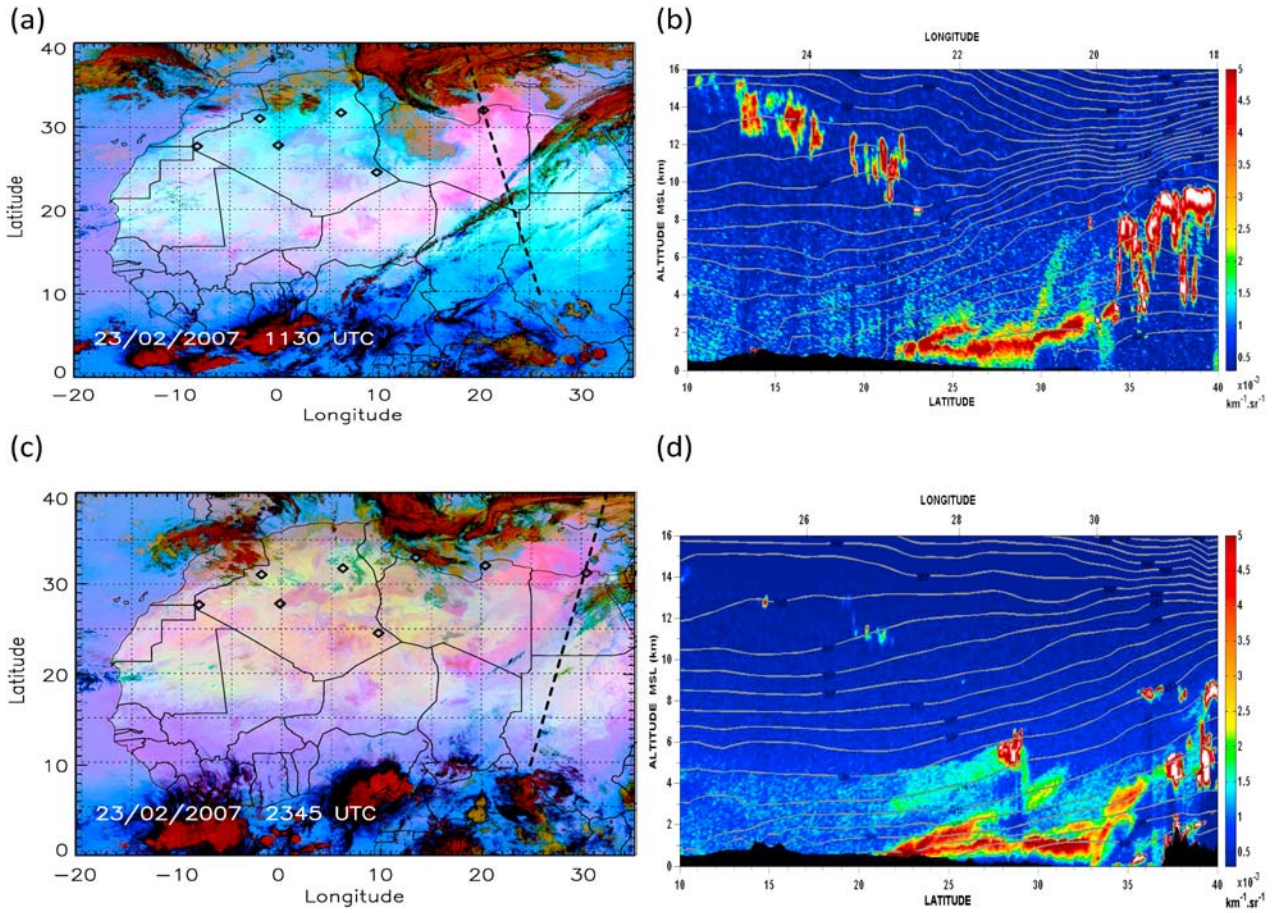

Figure 12. (a) Same as Figure 10a, but for 23 February 2007 at 1130 UTC. (b) Same as Figure 10b, but for 23 February 2007 at 1159 UTC CALIPSO observations and 1200 UTC ECMWF analysis. (c) Same as Figure 10a, but for 23 February 2007 at 2345 UTC. (d) Same as Figure 10b, but for 24 February 2007 at 0010 UTC.

[61] On 22 February at 1200 UTC, the simulated AOD field was in good agreement with the observed one. Particularly, the high AOD values (2.5) observed near the center of the cyclone (Figure 9a) were fairly replicated by the model (Figure 9b). However, the model underestimated by 0.25 the AODs associated with the plume of dust located over Libya (Figures 9a and 9b).

[62] Comparison with MSG-SEVIRI suggested that the model simulated reasonably the structure of the cyclone as well as its location, lifetime, trajectory and its associated dust transport over the study period (not shown). Furthermore, the OMI AI on 21 February at 1200 UTC shows high values (in excess of 3) over southern Algeria (Figure 8b) that corresponds to high dust concentrations (in excess of 8 g m^{-2}) simulated by the model (Figure 8d). The position and structure of the cyclone observed on 22 February on the OMI AI field (Figure 9b) were also reproduced by Meso-NH and were associated with a vertically integrated dust mass of about 9 g m^{-2} (Figure 9d). The dust transport over the Mediterranean Sea seen on the OMI observations to be associated with AI of 3 was replicated by the model and represented a vertically integrated dust mass on the order of 1.5 g m^{-2} (Figure 9d).

[63] Additionally, the model was able to reproduce the vertical distribution of clouds and dust described earlier using CALIPSO-CloudSat observations. The simulated dust concentrations and cloud fraction along the A-Train night orbit on 23 February 2007 at 0100 UTC are shown in Figure 11b. The altitude and the position of the dust clouds observed on CALIPSO (Figure 11b) were well reproduced by the model (Figure 11b). Also, the position and the altitude of the clouds seen on the CloudSat observations (Figure 11c) were well replicated by the model (Figure 11b).

[64] Furthermore, the model shows dust concentrations on the order of 200 μg m^{-3} below the elevated clouds (i.e., 34–40°N between 2 and 8 km; see Figured 11b and 11c). The presence of dust underneath the cloud top cannot be seen in the CALIPSO observations (Figure 11b) due to the attenuation of the lidar signal by the clouds. In the simulation, dust aerosols are present at the altitude of the clouds, due to the fact that the model does not account for the dust loss processes by the aqueous phase (only scavenging by rain below the cloud).

7.2. Simulated Dust Emissions

[65] Over the study period, dust mass fluxes on the order of 0.4–0.8 μg m^{-2} s^{-1} were simulated by Meso-NH to be

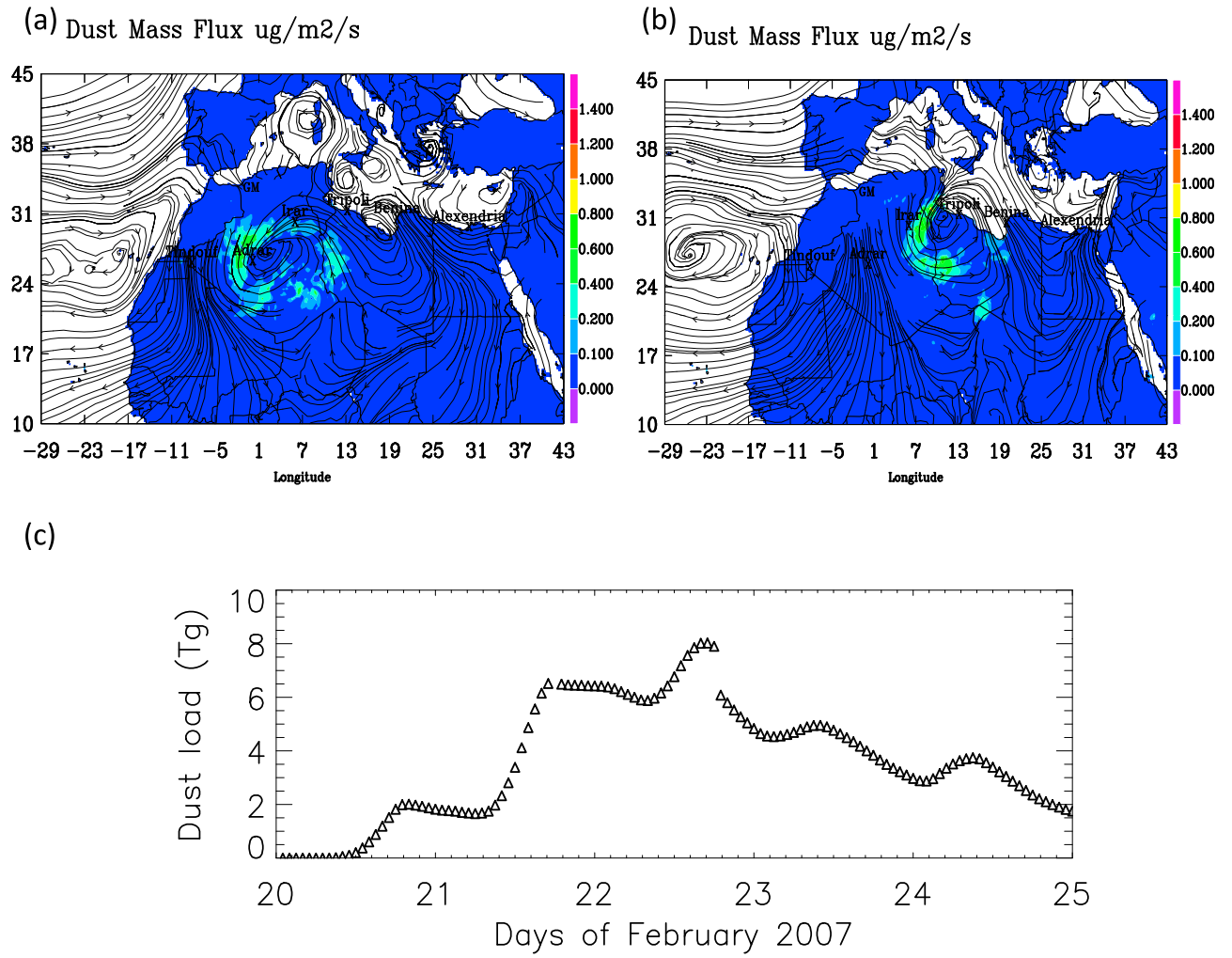

Figure 13. Dust Mass flux simulated by MesoNH (a) on 21 February 2007 at 1300 UTC and (b) on 22 February at 1300 UTC. The wind direction at 925 hPa is represented by the superimposed streamlines. (c) The temporal evolution of the dust load over North Africa derived by Meso-NH.

associated with the Saharan cyclone. The highest dust mass flux was simulated on 21 and 22 February when the cyclone was over Algeria and Libya (Figure 13).

[66] Figure 13c shows the temporal evolution of the mean dust load computed over the area impacted by the cyclone. The mean dust loads were obtained by considering only the area where the vertically integrated dust mass is higher than 0.5 g m^{-2}. This threshold was chosen in order to take into account only the region covered by dust in connection with the cyclone. The estimated daily mean dust loads during this event varied between 2 and 8 Tg (Figure 13c). The dust load started increasing substantially on 21 February around noon and reached its highest value (8 Tg) in the afternoon of 22 February, when the depression was over central Algeria (Figure 13c). In the evening of 22 February, the dust load started decreasing and was about 5 Tg in the morning of 23 February. This relatively rapid decrease in dust load is in coincidence with the development of deep convective clouds over the northern sector of the cyclone as suggested by the SEVIRI composite images (i.e., Figure 11a). The formation of deep clouds that occurred during this event, as the cyclone approached the Mediterranean cost, may have favored the scavenging by rain of large amounts of the dust present in the atmosphere. Furthermore, the center of the Sharav cyclone as well as part of the cold front was over the Mediterranean Sea, thereby leading to less near-surface dynamical forcing and hence dusts emissions. During the following day, the dust load associated with the cyclone now located mostly over the Mediterranean Sea continued to decline mainly because of the deposition, on one hand, and the reduction of the emissions on the other hand, and was on the order of 4 Tg on 24 February (Figure 13c). In addition to the day-to-day variability, a diurnal variation of the dust load can be seen during the days of relatively low dust loads (i.e., 23 and 24 February) with a maximum in the morning hours around 1000 UTC (Figure 13c).

8. Discussion and Conclusions

[67] The dust activity accompanying a Saharan depression over North Africa has been investigated. The development of the cyclone was favored by strong meridional temperature gradient and initiated on the lee side of the Atlas Mountains. A strong and highly mobile Subtropical Jet triggered the

development of the cyclone within this region of strong low-level baroclinity.

[68] The ECMWF analyses enabled the description of the structure of the cyclone. They showed a Saharan depression of a horizontal scale at the surface of 800–1000 km and a vertical extent of 8 km in altitude. The depression was characterized by a potential vorticity of about 2 PVU at its center and a surface pressure anomaly of 9 hPa. Ground-based measurements at different meteorological stations over North Africa allowed the characterization of the cyclone: Its warm front was marked at the surface by an increase in temperature of 5°C, its cold front was typified at the surface by a drop in temperature of 8°C and an increase in 10 m wind speed of 15 m s^{-1} and in its center, 10 m wind speeds were less than 3 m s^{-1} and strong ascent (in excess of 0.20 m s^{-1}) was present.

[69] The cyclone and its associated cold front were the major dynamic features that mobilized and transported the dust during this event. Important dust emissions occurred as the cyclone cold front and their associated strong surface winds (~25 m s^{-1}) cross over Algeria, Mali, Libya and Egypt. Dust emission was then followed by an upward mixing to high altitudes (~3 km) and by a cyclonic transport all around the eye of the cyclone. During its movement across the continent, the cyclone continued to produce dust locally in addition to the transported dust air masses. The dust storm was associated with dramatic visibility conditions with 0 km visibility rates at different locations and for more than 1 day.

[70] Furthermore, the cyclone cloud band observed along its northwestern edge was composed mostly of cirrus during the first 2 days of the cyclogenesis and reached 8 km in altitude. At a later stage, deep moist convection was reported in the MSG-SEVIRI and CloudSat observations with cloud tops reaching 10 km altitude.

[71] A numerical simulation was carried out with the Meso-NH model in order to estimate the dust emission associated with this event. The model was able to reproduce reasonably well the spatiotemporal evolution of the dust storm as well as the vertical distribution of dust and clouds associated with the cyclone. However, the model underestimated by 0.25 the AOD associated with the dust storm with respect to the MODIS deep blue AODs. Also, the model showed discrepancies in replicating the strong surface winds associated with the cyclone cold front. This could be due to the relatively coarse horizontal resolution at which the simulation was carried out (i.e., 25 km).

[72] The mean dust loads over the cyclone area were simulated to range between 2 and 8 Tg during the study period. This represents a large amount of dust compared to what was discussed in previous studies concerned with dust emissions. For example, the daily averaged dust loads derived downstream of the Bodélé depression are estimated to be on the order of 2.7 Tg [*Todd et al.*, 2008b], while those associated with emissions at the leading edge of the African monsoon flow [see *Bou Karam et al.*, 2008] are estimated to range between 0.5 and 0.8 Tg [*Bou Karam et al.*, 2009b]. Finally the dust loads associated with dry cyclones in the Intertropical Discontinuity region are estimated to be on the order of 0.4 Tg [*Bou Karam et al.*, 2009a]. Hence, Saharan cyclones may contribute significantly to the total dust load over West and North Africa observed annually. Further investigation is needed to substantiate these findings, in particular the annual frequency of Saharan cyclones over northern Africa and its correlation with the annual dust activity need to be addressed in future studies in order to evaluate the contribution of the highlighted mechanism to the total dust production over Africa north of the Equator.

[73] The high dust loads associated with the cyclone during its lifetime and along its trajectory are also likely to impact the radiative and energy budget over northern Africa at regional scale, and possibly the atmospheric dynamics in that region. Hence, future work will have to address the radiative impact of dust on the dynamical structure of the cyclone and its lifetime. This is particularly important over the Sahara (but also in other desertic regions) where the radiative impact of dust in the lower troposphere are conducive to conditions favorable for unexpectedly strong cyclogenesis in spite of the lack of moisture over these regions [e.g., *Chen et al.*, 1995].

[74] **Acknowledgments.** MODIS, OMI, and CloudSat observations used in this study were produced with the Giovanni online data system, developed and maintained by the NASA Goddard Earth Sciences (GES) Data and Information Services Center (DISC). The authors wish to thank SATMOS, ICARE, and Climserv for providing SEVIRI and CALIPSO data. The Department of Atmospheric Science at the University of Wyoming, especially L. Oolman, is acknowledged. D. Bou Karam's work on this study was supported by the Centre National des Etudes Spatiales (CNES), and the authors wish to thank particularly D. Renaut and C. Deniel. Finally, B. Francis is acknowledged for his help on data processing.

References

Alfaro, S. C., and L. Gomes (2001), Modelling mineral aerosol production by wind erosion: Emission intensities and aerosol size distributions in source areas, *J. Geophys. Res.*, *106*, 18,075–18,084, doi:10.1029/2000JD900339.

Alpert, P., and B. Ziv (1989), The Sharav cyclone: Observations and some theoretical considerations, *J. Geophys. Res.*, *94*, 18,495–18,514, doi:10.1029/JD094iD15p18495.

Alpert, P., B. I. Neeman, and Y. Shay-el (1990), Climatological analysis of Mediterranean cyclones using ECMWF data, *Tellus Ser. A*, *42*, 65–77.

Barkan, J., P. Alpert, H. Kutiel, and P. Kishcha (2005), Synoptics of dust transportation day from Africa toward Italy and central Europe, *J. Geophys. Res.*, *110*, D07208, doi:10.1029/2004JD005222.

Bartholy, J., R. Pongrácz, and M. Pattantyús-Ábrahám (2008), Analyzing the genesis, intensity, and tracks of western Mediterranean cyclones, *Theor. Appl. Clim.*, *96*(1), 133–144.

Bechtold, P., E. Bazile, F. Guichard, P. Mascart, and E. Richard (2001), A mass-flux convection scheme for regional and global models, *Q. J. R. Meteorol. Soc.*, *127*, 869–886, doi:10.1002/qj.49712757309.

Bou Karam, D., C. Flamant, P. Knippertz, O. Reitebuch, P. Pelon, M. Chong, and A. Dabas (2008), Dust emissions over the Sahel associated with the West African Monsoon inter-tropical discontinuity region: A representative case study, *Q. J. R. Meteorol. Soc.*, *134*, 621–634, doi:10.1002/qj.244.

Bou Karam, D., C. Flamant, P. Tulet, M. C. Todd, J. Pelon, and E. Williams (2009a), Dry cyclogenesis and dust mobilization in the intertropical discontinuity of the West African Monsoon: A case study, *J. Geophys. Res.*, *114*, D05115, doi:10.1029/2008JD010952.

Bou Karam, D., C. Flamant, P. Tulet, J.-P. Chaboureau, A. Dabas, and M. C. Todd (2009b), Estimate of Sahelian dust emissions in the intertropical discontinuity region of the West African Monsoon, *J. Geophys. Res.*, *114*, D13106, doi:10.1029/2008JD011444.

Cavazos, C., M. C. Todd, and K. Schepanski (2009), Numerical model simulation of the Saharan dust event of 6–11 March 2006 using the Regional Climate Model version 3 (RegCM3), *J. Geophys. Res.*, *114*, D12109, doi:10.1029/2008JD011078.

Chaboureau, J.-P., P. Tulet, and C. Mari (2007), Diurnal cycle of dust and cirrus over West Africa as seen from Meteosat Second Generation satellite and a regional forecast model, *Geophys. Res. Lett.*, *34*, L02822, doi:10.1029/2006GL027771.

Chen, S.-J., Y.-H. Kwo, W. Ming, and H. Ying (1995), The effect of dust radiative heating on low-level frontogenesis, *J. Atmos. Sci.*, *52*, 1414–1420, doi:10.1175/1520-0469(1995)052<1414:TEODRH>2.0.CO;2.

Chiapello, I., J. M. Prospero, J. Herman, and C. Hsu (1999), Detection of mineral dust over the North Atlantic Ocean and Africa with the Nimbus 7 TOMS, *J. Geophys. Res.*, *104*, 9277–9291, doi:10.1029/1998JD200083.

Cohard, J.-M., and J.-P. Pinty (2000), A comprehensive two-moment warm microphysical bulk scheme. ii: 2d experiments with non hydrostatic model, *Q. J. R. Meteorol. Soc.*, *126*, 1843–1859, doi:10.1256/smsqj.56614.

Crumeyrolle, S., L. Gomes, P. Tulet, A. Matsuki, A. Schwarzenboeck, and K. Crahan (2008), Increase of the aerosol hygroscopicity by aqueous mixing in a mesoscale convective system: A case study from the AMMA campaign, *Atmos. Chem. Phys.*, *8*, 6907–6924.

Cuesta, J., et al. (2008), Multiplatform observations of the seasonal evolution of the Saharan atmospheric boundary layer in Tamanrasset, Algeria, in the framework of the African Monsoon Multidisciplinary Analysis field campaign conducted in 2006, *J. Geophys. Res.*, *113*, D00C07, doi:10.1029/2007JD009417.

Cuesta, J., J. Marsham, D. J. Parker, and C. Flamant (2009a), Dynamical mechanisms controlling the vertical redistribution of dust and the thermodynamic structure of the West Saharan Atmospheric Boundary Layer during Summer, *Atmos. Sci. Lett.*, *10*, 34–42, doi:10.1002/asl.207.

Cuesta, J., C. Lavaysse, C. Flamant, M. Mimouni, and P. Knippetz (2009b), Northward bursts of the West African monsoon leading to rainfall over the Hoggar massif, Algeria, *Q. J. R. Meteorol. Soc.*, *136*, 174–189, doi:10.1002/qj.439.

Dayan, U., J. L. Heffter, J. M. Miller, and G. Gutman (1991), Dust intrusion events into the Mediterranean basin, *J. Appl. Meteorol.*, *30*, 1185–1199, doi:10.1175/1520-0450(1991)030<1185:DIEITM>2.0.CO;2.

Egger, J., P. Alpert, A. Tafferner, and B. Ziv (1995), Numerical experiments on the genesis of Sharav cyclones: Idealized simulations, *Tellus Ser. A*, *47*, 162–174.

Elfandy, M. G. (1940), The formation of depressions of the Khamsin type, *Q. J. R. Meteorol. Soc.*, *66*, 325–335.

Engelstaedter, S., I. Tegen, and R. Washington (2006), North African dust emissions and transport, *Earth Sci. Rev.*, *79*, 73–100, doi:10.1016/j.earscirev.2006.06.004.

Erel, Y., U. Dayan, R. Rabi, Y. Rudich, and M. Stein (2006), Trans boundary transport of pollutants by atmospheric mineral dust, *Environ. Sci. Technol.*, *40*, 2996–3005, doi:10.1021/es051502l.

Fan, S.-M., L. W. Horowitz, H. Levy II, and W. J. Moxim (2004), Impact of air pollution on wet deposition of mineral dust aerosols, *Geophys. Res. Lett.*, *31*, L02104, doi:10.1029/2003GL018501.

Fernandez-Partagas, J., D. M. Helgren, and J. M. Prospero (1986), Threshold wind velocities for raising dust in the western Sahara Desert, *ARO Tech. Rep. 19 684.3-GS*, U.S. Army Res. Lab., Army Res. Off., Adelphi, Md.

Flamant, C., J. P. Chaboureau, D. P. Parker, C. M. Taylor, J. P. Cammas, O. Bock, F. Timouk, and J. Pelon (2007), Airborne observations of the impact of a convective system on the planetary boundary layer thermodynamics and aerosol distribution in the intertropical discontinuity region of the West African Monsoon, *Q. J. R. Meteorol. Soc.*, *133*, 1175–1189, doi:10.1002/qj.97.

Grini, A., P. Tulet, and L. Gomes (2006), Dusty weather forecasts using the MesoNH mesoscale atmospheric model, *J. Geophys. Res.*, *111*, D19205, doi:10.1029/2005JD007007.

Hare, F. K. (1943), Atlas lee depressions and their significance for Scirocco, *Synoptic Div. Tech. Memo. 43*, 24 pp., U.K. Meteorol. Off., Exeter, U. K.

Hastenrath, S. (1991), *Climate Dynamics of the Tropics*, 486 pp., Kluwer Acad., Boston, Mass.

Horvath, K., L. Fita, R. Romero, B. Ivancan-Picek, and I. Stiperski (2006), Cyclogenesis in the lee of the Atlas Mountains: A factor separation numerical study, *Adv. Geosci.*, *7*, 327–331.

Hoskins, B. J., M. E. McIntyre, and A. W. Robsertson (1985), On the use and significance of isentropic potential vorticity maps, *Q. J. R. Meteorol. Soc.*, *111*, 877–946, doi:10.1256/smsqj.47001.

Intergovernmental Panel on Climate Change (IPCC) (2001), *Climate Change 2001: The Scientific Basis, Contribution of Working Group I to the Third Assessment Report of the Intergovernmental Panel on Climate Change*, edited by J. T. Houghton et al., Cambridge Univ. Press, New York.

Jankowiak, I., and D. Tanré (1992), Satellite climatology of Saharan dust outbreaks: Method and preliminary results, *J. Clim.*, *5*, 646–656, doi:10.1175/1520-0442(1992)005<0646:SCOSDO>2.0.CO;2.

Knippertz, P. (2008), Dust emissions in the West African heat trough: The role of the diurnal cycle and of extratropical disturbances, *Meteorol. Z.*, *17*, 553–563, doi:10.1127/0941-2948/2008/0315.

Knippertz, P., and A. H. Fink (2006), Synoptic and dynamic aspects of an extreme springtime Saharan dust outbreak, *Q. J. R. Meteorol. Soc.*, *132*, 1153–1177, doi:10.1256/qj.05.109.

Knippertz, P., C. Deutscher, K. Kandler, T. Müller, O. Schulz, and L. Schütz (2007), Dust mobilization due to density currents in the atlas region: Observations from the SAMUM 2006 field campaign, *J. Geophys. Res.*, *112*, D21109, doi:10.1029/2007JD008774.

Knippertz, P., et al. (2009), Dust mobilization and transport in the northern Sahara during SAMUM 2006: A meteorological overview, *Tellus Ser. B*, *61*, 12–31, doi:10.1111/j.1600-0889.2008.00380.x.

Lafore, J. P., et al. (1998), The Meso-NH atmospheric simulation system. Part I: Adiabatic formulation and control simulations, *Ann. Geophys.*, *16*, 90–109, doi:10.1007/s00585-997-0090-6.

Laurent, B., B. Marticorena, G. Bergametti, J. F. Léon, and N. M. Mahowald (2008), Modeling mineral dust emissions from the Sahara desert using new surface properties and soil database, *J. Geophys. Res.*, *113*, D14218, doi:10.1029/2007JD009484.

Lee, I. Y. (1983), Simulation of transport and removal processes of the Saharan dust, *J. Clim. Appl. Meteorol.*, *22*, 632–639, doi:10.1175/1520-0450(1983)022<0632:SOTARP>2.0.CO;2.

Lee, T. P.-J., S. R. Silberberg, and L. F. Bosart (1988), A case study of a severe winter storm in the Middle East, *Q. J. R. Meteorol. Soc.*, *114*, 61–90, doi:10.1002/qj.49711447904.

Moulin, C., et al. (1998), Satellite climatology of African dust transport in the Mediterranean atmosphere, *J. Geophys. Res.*, *103*, 13,137–13,144, doi:10.1029/98JD00171.

Noilhan, J., and J. F. Mahfouf (1996), The ISBA land surface parameterization scheme, *Global Planet. Change*, *13*, 145–159, doi:10.1016/0921-8181(95)00043-7.

Pedgley, D. E. (1972), Desert depression over north-east Africa, *Meteorol. Mag.*, *01*, 228–244.

Péwé, T. L. (1981), Desert dust: An overview, *Spec. Paper Geol. Soc. Am.*, *186*, 1–10.

Pierangelo, C., A. Chédin, S. Heilliette, N. Jacquinet-Husson, and R. Armante (2004), Dust altitude and infrared optical depth from AIRS, *Atmos. Chem. Phys.*, *4*, 1813–1822.

Prezerakos, N. G., S. C. Michaelides, and A. S. Vlassi (1990), Atmospheric synoptic conditions associated with the initiation of north-west African depression, *Int. J. Climatol.*, *10*, 711–729, doi:10.1002/joc.3370100706.

Prodi, F., and G. Fea (1979), A case of transport and deposition of Saharan dust over the Italian peninsula and southern Europe, *J. Geophys. Res.*, *84*(C11), 6951–6960, doi:10.1029/JC084iC11p06951.

Prospero, J. M., P. Ginoux, O. Torres, S. E. Nicholson, and T. E. Gill (2002), Environmental characterization of global sources of atmospheric soil dust identified with the Nimbus 7 Total Ozone Mapping Spectrometer (TOMS) absorbing aerosol product, *Rev. Geophys.*, *40*(1), 1002, doi:10.1029/2000RG000095.

Reiter, E. R. (1975), Handbook for forecasters in the Mediterranean, *Tech. Pap. 5–75*, 344 pp., Nav. Postgrad. Sch., Monterey, Calif.

Schepanski, K., I. Tegen, B. Laurent, B. Heinold, and A. Macke (2007), A new Saharan dust source activation frequency map derived from MSG-SEVIRI IR channels, *Geophys. Res. Lett.*, *34*, L18803, doi:10.1029/2007GL030168.

Schepanski, K., et al. (2009), Meteorological processes forcing Saharan dust emission inferred from MSG-SEVIRI observations of sub-daily dust source activation and numerical models, *J. Geophys. Res.*, *114*, D10201, doi:10.1029/2008JD010325.

Stephens, G. L., et al. (2002), The CloudSat mission and the A-Train, *Bull. Am. Meteorol. Soc.*, *83*, 1771–1790, doi:10.1175/BAMS-83-12-1771.

Stephens, G. L., et al. (2008), CloudSat mission: Performance and early science after the first year of operation, *J. Geophys. Res.*, *113*, D00A18, doi:10.1029/2008JD009982, [printed 114(D8), 2009].

Tantawy, A. H. I. (1964), The role of the jet stream in the formation of desert depressions in the Middle East, *WMO Tech. Note 64*, pp. 159–171, World Meteorol. Organ., Geneva.

Thorncroft, C. D., and H. A. Flocas (1997), A case study of Saharan cyclogenesis, *Mon. Weather Rev.*, *125*, 1147–1165, doi:10.1175/1520-0493(1997)125<1147:ACSOSC>2.0.CO;2.

Todd, M. C., R. Washington, S. Raghavan, G. Lizcano, and P. Knippertz (2008a), Regional model simulations of the Bodélé low-level jet of northern Chad during the Bodélé Dust Experiment (BoDEx 2005), *J. Clim.*, *21*, 995–1012, doi:10.1175/2007JCLI1766.1.

Todd, M. C., et al. (2008b), Quantifying uncertainty in estimates of mineral dust flux: An inter-comparison of model performance over the Bodélé Depression, northern Chad, *J. Geophys. Res.*, *113*, D24107, doi:10.1029/2008JD010476.

Trigo, I. F., T. D. Davies, and G. R. Bigg (1999), Objective climatology of cyclones in the Mediterranean region, *J. Clim.*, *12*, 1685–1696, doi:10.1175/1520-0442(1999)012<1685:OCOCIT>2.0.CO;2.

Trigo, I. F., G. R. Bigg, and T. D. Davies (2002), Climatology of Cyclogenesis mechanisms in the Mediterranean, *Mon. Weather Rev.*, *130*, 549–569, doi:10.1175/1520-0493(2002)130<0549:COCMIT>2.0.CO;2.

Tulet, P., V. Crassier, F. Cousin, K. Suhre, and R. Rosset (2005), ORILAM, a three moment lognormal aerosol scheme for mesoscale atmospheric model: Online coupling into the Meso-NH-C model and validation on the Escompte campaign, *J. Geophys. Res.*, *110*, D18201, doi:10.1029/2004JD005716.

Tulet, P., M. Mallet, V. Pont, J. Pelon, A. Boone (2008), The 7–13 March 2006 dust storm over West Africa: Generation, transport and vertical stratification, *J. Geophys. Res.*, *113*, D00C08, doi:10.1029/2008JD009871.

Washington, R., and M. C. Todd (2005), Atmospheric controls on mineral dust emission from the Bodélé Depression, Chad: The role of the low level jet, *Geophys. Res. Lett.*, *32*, L17701, doi:10.1029/2005GL023597.

Westphal, D. L., O. B. Toon, and T. N. Carlson (1985), A numerical investigation of Saharan dust storms, Ph. D. thesis, Penn. State Univ., Univ. Park.

Winker, D. M., J. Pelon, and M. P. McCormick (2003), The CALIPSO mission: Spaceborne lidar for observation of aerosols and clouds, *Proc. SPIE*, *4893*, 1–11.

Winstanley, D. (1970), The North African flood disaster September 1969, *Weather*, *25*, 390–403.

Zender, C., H. Bian, and D. Newman (2003), The mineral dust entrainment and deposition model DEAD: Description and 1990s dust climatology, *J. Geophys. Res.*, *108*(D14), 4416, doi:10.1029/2002JD002775.

D. Bou Karam, C. Flamant, and J. Pelon, LATMOS, IPSL, Université Pierre et Marie Curie, CNRS, 4 Pl. Jussieu, Paris F-75252, France. (diana.boukaram@latmos.ipsl.jussieu.fr)

J. Cuesta, LMD, IPSL, Ecole Polytechnique, CNRS, Palaiseau F-91128, France.

E. Williams, Parsons Laboratory, Massachusetts Institute of Technology, Cambridge, MA 02139, USA.